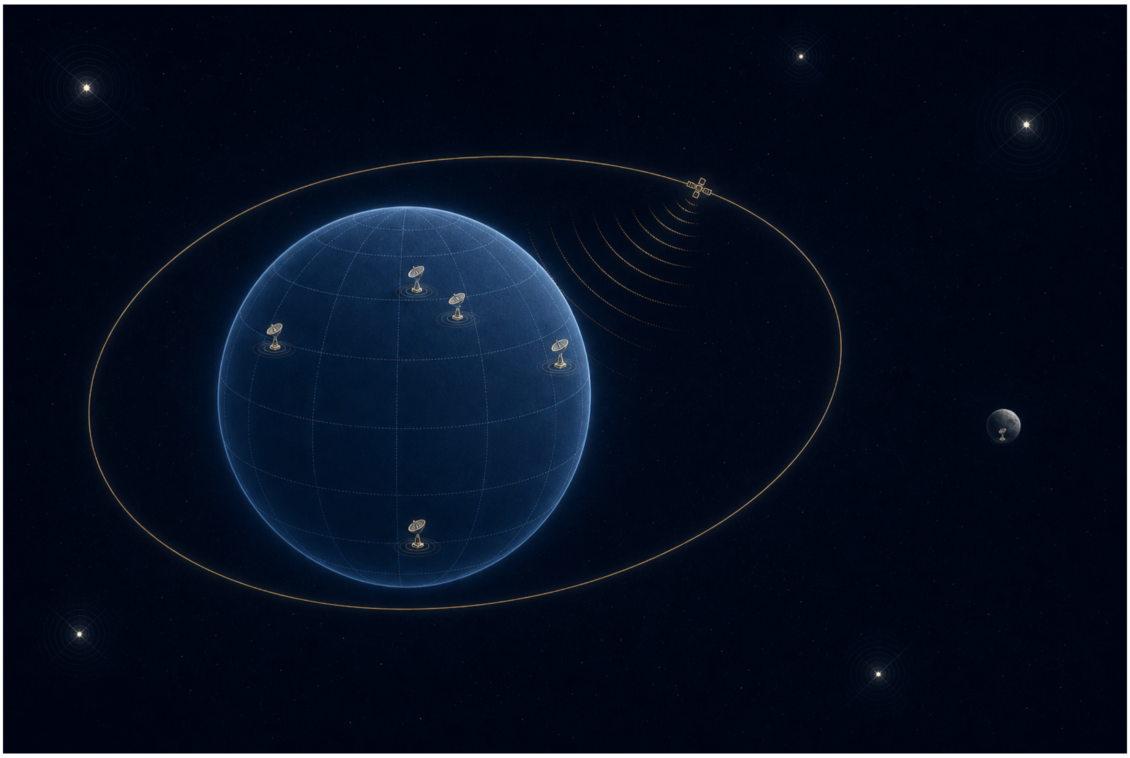

VLBI with earth-orbiting transmitters

Evaluation of Artificial-Source VLBI Observing Plans for VGOS

Master's thesis in Department of Physics and Astronomy

HE QIN
YIZHOU WANG

Department of Physics and Astronomy
CHALMERS UNIVERSITY OF TECHNOLOGY
Gothenburg, Sweden 2026
www.chalmers.se

Master's thesis 2026

VLBI with earth-orbiting transmitters

Evaluation of Artificial-Source VLBI Observing Plans for VGOS

HE QIN
YIZHOU WANG

Department of Physics and Astronomy
Onsala Space Observatory
Chalmers University of Technology
Gothenburg, Sweden 2026

VLBI with earth-orbiting transmitters
Evaluation of Artificial-Source VLBI Observing Plans for VGOS
HE QIN
YIZHOU WANG

Supervisor: Rüdiger Haas, Department of Physics and Astronomy
Examiner: Rüdiger Haas, Department of Physics and Astronomy

Master's Thesis 2026
Department of Physics and Astronomy
Onsala Space Observatory
Chalmers University of Technology
SE-412 96 Gothenburg
Telephone +46 31 772 1000

Cover: Scientific illustration of artificial VLBI transmitters observed by a VGOS station network.

Typeset in LaTeX
Printed by Chalmers Reproservice
Gothenburg, Sweden 2026

VLBI with earth-orbiting transmitters
Evaluation of Artificial-Source VLBI Observing Plans for VGOS
HE QIN
YIZHOU WANG
Department of Physics and Astronomy
Chalmers University of Technology

Abstract

Geodetic very long baseline interferometry (VLBI) mainly observes distant AGN sources. However, natural radio sources are uncontrollable and therefore cannot fully satisfy the future space-geodetic demand for controllable near-field signals. This study investigates the feasibility of the Genesis near-Earth satellite source, the NovaMoon lunar-surface transmitter, and observing plans involving artificial sources and AGN sources. By combining Python-based physical simulation, VieSched++ observation scheduling, and VieVS simulation, the observation potential of artificial VLBI transmitter sources within a VGOS network is evaluated.

The Python simulations show that Genesis requires relatively low transmission power, but its rapid apparent motion makes it more sensitive to transmitter phase-centre errors. NovaMoon provides more stable common-view geometry, but the lunar distance significantly increases the link-budget requirements. The VieSched++ results indicate that expanding the station network substantially improves station and baseline coverage, while the inclusion of AGN sources shifts the observation plans from artificial-source-dominated structures toward reference-source-dominated configurations. The VieVS results further demonstrate that the five-station artificial-source schedules provide insufficient station-coordinate stability. Genesis exhibits clear improvement within the sixteen-station network, whereas the NovaMoon-only schedule remains limited by geometric conditions, and the AGN-containing sixteen-station schedules provide the most stable overall geodetic performance. Overall, the feasibility of artificial VLBI transmitter sources depends not only on signal-link and visibility conditions, but also on the combined effects of source-type configuration, station-network geometry, and scheduling structure.

Keywords: VLBI, VGOS; Genesis, NovaMoon, artificial radio source, VieSched++, VieVS, observation plans, link budget, AGN.

Acknowledgements

On the occasion of the completion of this thesis, we would like to express our sincere gratitude to everyone who has given us help, support, and encouragement during our studies and research.
First of all, we would like to express our special thanks to our supervisor and examiner, Professor Rüdiger Haas. During the process of choosing the thesis topic, developing the research ideas, designing the methods, and writing the thesis, he gave us patient guidance and valuable advice. Each discussion helped us clarify the research direction and gain a deeper understanding of the topic. His rigorous academic attitude and responsible working style have been very important for the completion of this thesis, and we have benefited a lot from this experience.
At the same time, we would also like to thank each other as teammates. Throughout the thesis project, we discussed problems together, divided the work, cooperated with each other, and supported each other. When we encountered difficulties and uncertainties, good communication and teamwork helped us complete our own parts better and made the whole thesis process smoother.
We would also like to acknowledge the developers and maintainers of the Vienna VLBI and Satellite Software open-source projects, especially VieSched++ and VieVS. These software tools provided an important basis for the VLBI scheduling analysis and related calculations in this thesis, and allowed us to carry out this study based on established professional tools.
In addition, we would like to thank the instructors of the courses Satellite positioning - RRY095 and Satellite communications - RRY100, Professor Jan Johansson and Professor Rüdiger Haas. These courses provided us with important theoretical foundations in satellite positioning, satellite communications, link budget, and space observation, which supported the development of this thesis.
We would also like to thank our families and friends. We are grateful for their understanding, support, and encouragement in our studies and daily life. Whether things went smoothly or we faced pressure and difficulties, their care and support always gave us the strength to keep going. Their long-term support allowed us to focus on our studies in Sweden and complete this thesis with peace of mind.
Additionally, He Qin would like to give special thanks to Jiayi Tang for her friendship and encouragement, which helped him get through the days of uninspiring food and limited sunshine. He sincerely wishes her all the best in the future.
Finally, we would like to thank Chalmers University of Technology for providing us with a good learning environment and academic resources. Our study experience here has not only improved our professional knowledge, but also broadened our horizons. It has helped us grow in academic thinking, independent research ability, and cross-cultural communication.
We would like to express our sincere thanks to everyone who has helped and supported us during this journey.

He Qin and Yizhou Wang, Gothenburg

List of Acronyms

Below is the list of acronyms that have been used throughout this thesis listed in alphabetical order:

AGN	Active Galactic Nucleus
CRF	Celestial Reference Frame
DORIS	Doppler Orbitography and Radiopositioning Integrated by Satellite
ECEF	Earth-Centred, Earth-Fixed
ECI	Earth-Centred Inertial
EIRP	Equivalent Isotropically Radiated Power
EOP	Earth Orientation Parameters
ESA	European Space Agency
Genesis	ESA mission concept for co-location of geodetic techniques in space
GNSS	Global Navigation Satellite System
LOS	Line of Sight
PCO	Phase Centre Offset
PCV	Phase Centre Variation
SEFD	System Equivalent Flux Density
SLR	Satellite Laser Ranging
SNR	Signal-to-Noise Ratio
TLE	Two-Line Element set
TRF	Terrestrial Reference Frame
VGOS	VLBI Global Observing System
VLBI	Very Long Baseline Interferometry

Nomenclature

Below is the nomenclature of indices, parameters, and variables that are planned to be used throughout this thesis.

Indices

i,j	Indices for VLBI stations or baselines
k	Index for frequency band
t	Time or simulation epoch

Sets

$\mathcal{S}$	Set of ground stations
$\mathcal{B}$	Set of baselines
$\mathcal{F}$	Set of frequency bands
$\mathcal{T}$	Set of simulation epochs or scheduling times

Parameters

c	Speed of light
f	Radio frequency
λ	Wavelength
Δt	Simulation time step
E_{min}	Minimum elevation angle
G	Antenna gain
L_{fs}	Free-space path loss
L_{atm}	Atmospheric attenuation
P_{t}	Transmit power

EIRP	Equivalent isotropically radiated power
SEFD	System equivalent flux density

Variables

$\mathbf{r}$	Position vector
$\mathbf{b}_{ij}$	Baseline vector between stations i and j
$\hat{\mathbf{s}}$	Unit line-of-sight vector
τ	Geometric or error delay
$\Delta\phi$	Phase error
N_{obs}	Number of observations
N_{scan}	Number of scans

Contents

List of Figures

List of Tables

1

Introduction

1.1 Background

Geodetic Very Long Baseline Interferometry (VLBI) is one of the fundamental space geodetic techniques for determining the celestial reference frame, the terrestrial reference frame, and Earth orientation parameters. In conventional geodetic VLBI, distant extragalactic radio sources are observed by a network of ground radio telescopes. Because these sources are located at extremely large distances, their incoming wavefronts can usually be treated as plane waves, which simplifies the geometric delay model.

However, conventional VLBI sources are natural radio sources. Their signal strength, sky distribution, and availability cannot be controlled by the observer. This motivates the investigation of artificial radio transmitters as complementary VLBI sources. Artificial transmitters placed on near-Earth satellites or on the lunar surface may provide controlled signals and new observation geometries. In particular, future concepts such as Genesis and lunar transmitters create the possibility of connecting VLBI observations with satellite-based space geodetic techniques.

1.2 Motivation for Artificial VLBI Transmitters

Artificial VLBI transmitters differ from traditional AGN sources in both geometry and signal properties. Genesis represents a rapidly moving near-Earth source, while Novamoon station represents a much more distant and slowly varying source. These differences influence the common-view windows between stations, the propagation distance, the required transmit power, and the scheduling behaviour of the observations.

Before such sources can be used in practical VLBI observing sessions, their feasibility must be assessed. A source may be visible to one station, but it is useful for VLBI only when it can be observed by at least two stations at the same time. In addition, sufficient signal strength must be available at both receiving stations, and the observation must still be schedulable when realistic constraints such as elevation limits, station slewing, scan duration, and source competition are considered.

Therefore, this thesis combines a Python-based physical simulation with VieSched++ scheduling experiments. The Python model is used to evaluate visibility, link budget, required EIRP or transmit power, and phase-centre-related effects. The VieSched++ model is used to test whether the physically favourable opportunities can also be used in practical observing schedules.

1.3 Aim and Research Questions

The aim of this thesis is to evaluate the feasibility of observing artificial VLBI transmitters with a selected VGOS station network. The study focuses on two artificial-source scenarios: the Genesis near-Earth transmitter and Novamoon station transmitter. Their performance is analysed using both Python-based physical simulations and VieSched++ scheduling experiments.

The main research questions are:

- What EIRP or transmit power is required for the Genesis and Novamoon station scenarios under the assumed VGOS receiving constraints?
- Which ground stations and baselines are most favourable in terms of visibility, common-view duration, and link budget?
- How do phase-centre offset and phase-centre variation affect the delay and phase behaviour of artificial-source VLBI observations?
- Are the station priorities obtained from the Python simulation consistent with the schedules generated by VieSched++?
- How does the inclusion of AGN sources affect the scheduling of artificial transmitters in mixed observing plans, and how does the mixed schedule compare with a pure AGN-only reference schedule?

1.4 Scope and Thesis Structure

This thesis is based on simulation studies and does not analyse real VLBI observation data. The artificial transmitters are modelled using simplified but controlled assumptions in order to compare their geometric visibility, link budget requirements, and phase-centre-related error behaviour. The station network is limited to selected VGOS station configurations, and the scheduling analysis is performed using seven VieSched++ observing plans: Genesis-5, NovaMoon-5, Genesis-16, NovaMoon-16, Genesis+NovaMoon-16, Genesis+NovaMoon+AGN-16, and AGN-16. The AGN-16 plan is used as a pure conventional AGN-only reference schedule for comparison with the mixed artificial-source and AGN schedule.

Chapter 2 introduces the theoretical background required for the study, including geodetic VLBI, artificial source types, VGOS scheduling, link budget, and phase- centre effects. Chapter 3 describes the Python simulation method. Chapter 4 presents the VieSched++ scheduling method. Chapter 5 gives the simulation, scheduling, and VieVS results, together with their interpretation. Chapter 6 summarises the main findings, discusses the implications and limitations of the study, and gives an outlook for future work.

2

Theoretical Background

2.1 Principles of Geodetic VLBI

Very Long Baseline Interferometry (VLBI) is based on observing the same radio signal at two or more widely separated stations. The fundamental observable is the difference in arrival time of the signal between stations. For a distant source, this delay is mainly determined by the projection of the baseline vector onto the source direction. If the baseline vector between two stations is denoted by $\mathbf{B}$ and the unit vector towards the source by $\mathbf{s}$, the geometric delay can be written in simplified form as

$$\tau_{\mathrm{g}} = \frac{\mathbf{B} \cdot \mathbf{s}}{c}, \tag{2.1}$$

where c is the speed of light. In practical geodetic VLBI, additional terms are required for Earth orientation, station motion, atmospheric propagation, clock offsets, and instrumental delays. However, the baseline projection remains the central geometric quantity.

In classical geodetic VLBI, the observed sources are usually extragalactic radio sources. Their distances are so large that the incoming wavefront can be treated as planar over the scale of the Earth. This far-field approximation makes the source direction effectively the same for all stations at a given time. In this case, the geometry is mainly controlled by the station baseline and the apparent celestial direction of the source.

Artificial transmitters are different. A transmitter on an Earth-orbiting satellite, such as Genesis, or a transmitter located near the Moon, such as NovaMoon, is a finite-distance source. Its apparent direction and range are not the same for all stations, and both change with time. The visibility of the source therefore depends on the transmitter position, the ground-station locations, the elevation mask, and the transmitter attitude. This is especially important for Earth-orbiting sources, where the apparent motion can be fast and the common-view windows can be short. For lunar-distance sources, the apparent motion is slower and the common-view windows can be longer, but the path loss is much larger.

For this reason, artificial-source VLBI must be evaluated using both interferometric geometry and radio-link feasibility. A source may be visible from two stations but still require a high transmitted power, or it may have a favourable link budget but produce large phase variations because of antenna phase-centre effects. The later analysis therefore separates the signal-strength problem from the delay-error problem.

2.2 VGOS Network and Observation Scheduling

The VLBI Global Observing System (VGOS) is designed to improve the precision and temporal resolution of geodetic VLBI. Compared with legacy VLBI systems, VGOS uses faster slewing antennas, broadband receiving systems, and observing strategies that aim to increase the number and quality of observations. The network geometry is important because different baselines provide different sensitivities to geodetic parameters and to local or source-related errors.

For artificial sources, the scheduling problem differs from normal AGN-based sessions. A natural radio source can often be selected from a large catalogue, and the scheduler can choose sources to improve sky coverage and station participation. An artificial source is instead constrained by its orbit or trajectory. It can only be observed when it is above the elevation limit at the required stations. A valid interferometric observation also requires common-view visibility, meaning that at least two stations can observe the source at the same time. If more stations are simultaneously available, the observation can generate more baselines and may be more useful for network analysis.

In this thesis, observability is used in two related but distinct senses. The first is radio-link observability: the transmitted signal must be strong enough at the receiving stations. This is evaluated through the link budget and the required EIRP or transmit power. The second is geodetic observability: the observation must be useful for VLBI analysis. This depends on common-view time, station participation, baseline geometry, elevation, and sensitivity to systematic errors. A favourable link budget therefore does not automatically imply a favourable geodetic observation.

Scheduling also introduces practical constraints. Antennas need time to slew between targets, observations have minimum and maximum scan lengths, and repeated observations of the same source must be distributed in time. In a mixed schedule with artificial sources and AGN sources, the artificial source can add new geometric information, but it can also remove time from normal AGN observations. This trade-off is one of the motivations for comparing Python-based visibility and error calculations with VieSched++ observing plans.

2.3 Genesis, NovaMoon, and AGN Sources

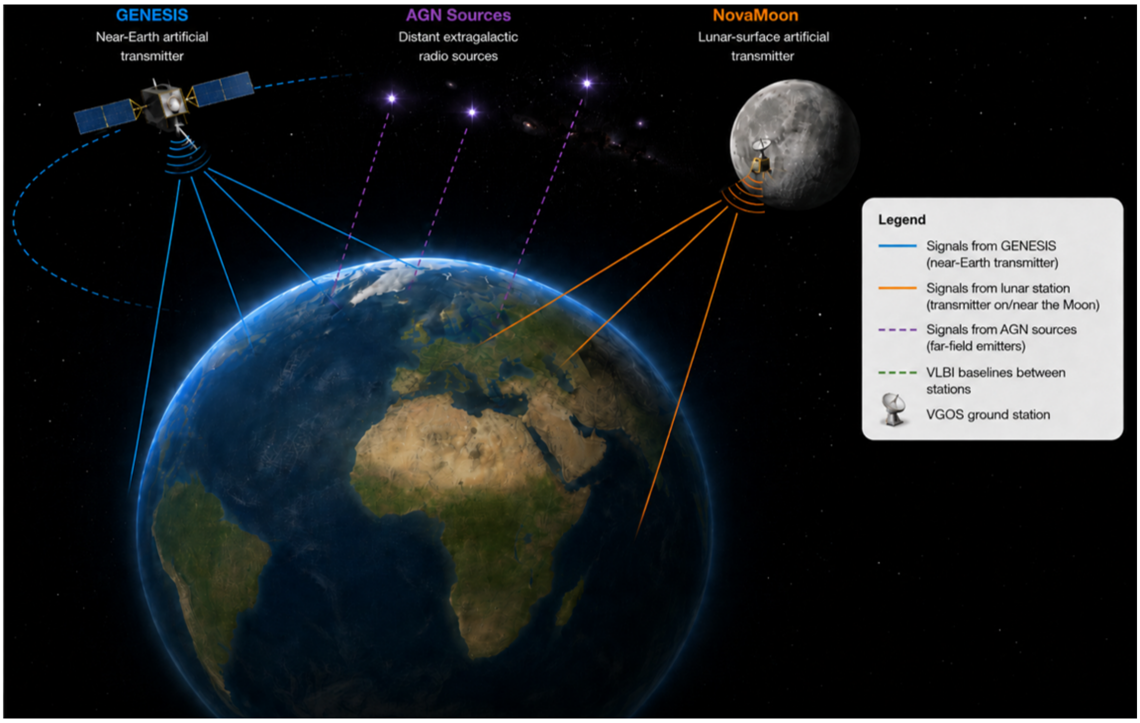

Figure 2.1: System Overview

The sources considered in this thesis represent three different observing regimes. AGN sources are natural far-field sources and form the standard reference case for geodetic VLBI. Genesis is an Earth-orbiting artificial transmitter and therefore has fast apparent motion and short visibility windows. NovaMoon represents a lunar-distance artificial transmitter, with slower apparent motion but much larger propagation distance.

Table 2.1: Conceptual comparison of the source types considered in this thesis.

Source type	Distance regime	Main role	Main limitation
AGN	Far field	Reference and mixed schedules	Source structure and flux variability.
Genesis	Earth orbit	Satellite artificial transmitter	Short common-view passes and attitude effects.
NovaMoon	Lunar distance	Lunar artificial transmitter	Large path loss and limited geometry.

This comparison is useful because the same VLBI network responds differently to each source type. For AGN observations, the main scheduling freedom is the choice of source direction on the sky. For Genesis, the source direction is determined by the satellite orbit and changes rapidly. For NovaMoon, the source is much farther away and changes more slowly, but the larger range strongly affects the required transmitted power. These differences explain why the thesis evaluates the Earth-orbiting and lunar cases separately before comparing them with schedules that also include AGN sources.

The artificial sources are not only alternative radio targets. They are also controlled transmitters, which means that their signal power, frequency bands, antenna pattern, and attitude can in principle be specified or modelled. This is an advantage compared with natural sources, but it also introduces transmitter dependent error sources. In particular, the position of the transmitting antenna phase centre and its variation with viewing direction become important when the signal is used for interferometric delay measurements.

2.4 Link Budget and Signal Observability

The link budget describes how the transmitted radio signal is reduced or modified before it reaches a receiving station. For an artificial transmitter, the link budget can be used in two directions. If the transmitted power is known, it can be used to estimate the received spectral flux density. Conversely, if a target received flux density is required, the link budget can be used to estimate the required equivalent isotropically radiated power (EIRP) or the actual transmit power after antenna gain is included.

The spectral flux density is commonly expressed in jansky (Jy), where

$$1\ \text{Jy} = 10^{-26}\ \text{W}\,\text{m}^{-2}\,\text{Hz}^{-1}. \tag{2.2}$$

Using a target value in Jy allows the artificial transmitter to be compared with radio sources used in VLBI observations. In this thesis, the Python simulations use a target flux-density level and calculate the EIRP and transmit power needed to reach that level at the receiving stations.

Several factors affect the required transmitted power. The largest basic term is the free-space path loss, which increases with both distance and frequency. This is why the lunar-distance case requires much larger EIRP than the Earth-orbiting case. The receiving station gain, the transmitter antenna gain, and the band-dependent wavelength also enter the calculation. In addition, practical losses such as polarisation mismatch, implementation loss, atmospheric attenuation, and off-boresight antenna loss can increase the required power.

Elevation angle is especially important. At low elevation, the signal travels through a longer atmospheric path and is more affected by atmospheric attenuation. Low-elevation observations can also be less favourable for geodetic analysis because they are more sensitive to atmospheric modelling errors. However, they may be necessary in order to increase common-view time, especially for artificial sources with limited visibility. The link budget therefore has to be interpreted together with the common-view geometry and the scheduling constraints.

In the results chapter, the best and worst link-budget values should therefore be understood as geometry-dependent quantities. A best case usually corresponds to a more favourable range, elevation, and antenna pointing condition, while a worst case can occur at low elevation or larger off-boresight angle. The link budget does not by itself determine whether a baseline is optimal for VLBI; it only answers whether the signal level can be made feasible under the assumed transmitter and propagation model.

2.5 Phase Centre Errors

For an ideal antenna, the transmitted or received signal could be treated as if it originated from a single fixed point. Real antennas do not behave exactly in this way. The effective phase centre can be offset from the mechanical reference point and can also vary with frequency and viewing direction. These effects are usually described using a phase-centre offset (PCO) and phase-centre variation (PCV).

The PCO is a fixed vector between the antenna reference point and the nominal phase centre. If the line-of-sight unit vector from the transmitter to a station is denoted by $\mathbf{u}$, the projection of the PCO vector $\mathbf{p}$ along the line of sight gives an approximate path contribution,

$$\Delta\rho_{\mathrm{PCO}} = \mathbf{p} \cdot \mathbf{u}. \tag{2.3}$$

For a VLBI baseline, the relevant quantity is not only the projection towards one station, but the difference between the projections towards the two stations. The phase-centre contribution to the baseline delay can therefore be written in simplified form as

$$\Delta\tau_{\mathrm{PCO}} = \frac{\mathbf{p} \cdot \mathbf{u}_1 - \mathbf{p} \cdot \mathbf{u}_2}{c}, \tag{2.4}$$

where $\mathbf{u}_1$ and $\mathbf{u}_2$ are the line-of-sight vectors from the transmitter to the two stations. This expression shows why the error depends on the differential viewing geometry. A longer baseline does not automatically produce a larger phase-centre error; the important factor is how differently the two stations view the transmitting antenna.

The PCV represents an additional direction-dependent phase-centre effect. It is usually smaller than the main PCO term but can still contribute to delay and phase variations. Since the viewing direction changes with time, especially for an Earth-orbiting transmitter, both PCO and PCV can lead to time-varying interferometric phase errors.

The phase error corresponding to a delay error $\Delta\tau$ at frequency f is

$$\Delta\phi = 2\pi f \Delta\tau. \tag{2.5}$$

This relation explains why the same delay error produces a larger phase error at higher frequency. It is also the reason why the X-band results in the later chapters show larger phase variations than the S-band results for the same baseline delay variation.

It is useful to distinguish between an absolute phase-centre induced delay and a pass-relative delay variation. A nearly constant delay bias over a short pass may be easier to absorb into calibration or parameter estimation, while a changing delay affects the phase stability within the observation interval. For this reason, the later simulations report phase-centre effects mainly as variations relative to the start of each common-view pass. This distinction is important when interpreting the Genesis results, where a baseline can have a favourable signal condition but still show a large phase-centre related delay variation.

2.6 Summary of Evaluation Criteria

The theoretical background leads to two main evaluation dimensions used in the rest of the thesis. The first is signal feasibility. It is described by common-view time, received flux-density target, EIRP, and transmit power. The second is interferometric stability. It is described by phase-centre induced delay and phase variation on each baseline.

A candidate artificial VLBI source is favourable only if both dimensions are acceptable. A strong signal is not sufficient if the observation is strongly affected by time-varying phase-centre errors. Similarly, a geometrically useful baseline is not practical if the required transmit power is too high. This combined view is used in Chapter 3 for the Python simulations, in Chapter 4 for the VieSched++ schedules, and in Chapter 5 for the comparison between Genesis, NovaMoon, and AGN-based observing plans.

3

Python Simulation Method

3.1 Overall Workflow of Python Simulation

The Python simulation in this chapter is used to establish a numerical evaluation method for the observational feasibility of artificial VLBI transmitter sources and to provide preliminary physical constraints for the subsequent VieSched++ scheduling analysis. The method evaluates the observation conditions of the Genesis satellite source and the NovaMoon lunar surface source under a given ground station network from three aspects: geometric visibility, link budget, and transmitter phase-centre error propagation. Through this simulation framework, available common-view time windows can be identified before entering the scheduling stage, the transmission conditions required to satisfy the target spectral flux density can be estimated, and the influence of transmitter antenna errors on VLBI delay and phase can be analysed.

Unlike conventional AGN sources, both Genesis and NovaMoon are located at finite distances, and their observation geometry cannot be approximated using a fixed far-field direction. For such artificial transmitter sources, different ground stations may have different line-of-sight directions, propagation distances, elevation angles, and atmospheric propagation paths at the same epoch. Therefore, this chapter first establishes the source position and attitude models and calculates the geometric relationship between the source and each ground station at each simulation epoch. This geometric relationship not only determines the dual-station common-view condition, but also further affects the propagation loss, antenna off-boresight gain, and the projection of phase-centre errors along different line-of-sight directions in the link budget.

The overall Python method consists of three interconnected model layers. The first layer is the near-field geometry and common-view model, which is used to determine whether an artificial source can be simultaneously observed by the two stations forming a VLBI baseline. For a baseline formed by stations i and j, an epoch is regarded as a valid common-view epoch only when both stations satisfy the minimum elevation constraint at the same epoch. This step filters the continuous time axis into common-view passes that can be used for the subsequent link budget and error propagation analysis.

$$\mathcal{C}_{ij}(t) = [e_i(t) \geq e_{\min}] \cap [e_j(t) \geq e_{\min}] \tag{3.1}$$

where $\mathcal{C}_{ij}(t)$ denotes the common-view status of baseline $i - j$ at time t, $e_i(t)$ and $e_j(t)$ are the elevation angles of the artificial source relative to the two stations, respectively, and $e_{\min}$ is the minimum elevation threshold. This condition reflects the dual-station constraint in artificial-source VLBI simulations: visibility at a single station is not equivalent to baseline observability, and the subsequent link budget and error propagation are performed only within dual-station common-view windows.

The second layer is the link budget model. This model is used to evaluate the required equivalent isotropically radiated power or transmit power of the artificial source when geometric common-view conditions have already been satisfied, so that the two receiving stations can simultaneously reach the target spectral flux density. This study adopts a reverse link budget method, which starts from the predefined target received signal strength and derives the required transmission conditions by considering the propagation distance, atmospheric attenuation, system losses, and antenna off-boresight gain. Since the distance, elevation angle, and atmospheric loss at the two stations of the same baseline are usually different, the transmission requirement of a baseline at a given epoch is determined by the stricter receiving constraint of the two stations. This treatment ensures that the same artificial source signal can simultaneously satisfy the receiving requirements at both ends of the baseline at that epoch. Therefore, the link budget model further converts the geometric common-view windows into a feasibility assessment of transmit power, antenna pointing, and propagation conditions.

The third layer is the transmitter phase-centre error propagation model. The antenna phase centre offset and phase centre variation of an artificial source are defined in the transmitter body coordinate system, while the VLBI observation error appears as a differential path error between the receiving paths of two ground stations. Therefore, the simulation first uses the source attitude model to transform the transmitter phase-centre error into the Earth-fixed coordinate system and then projects it onto the line-of-sight directions of the two stations. For a baseline, the difference between the two projected quantities forms the differential path error, which is further converted into delay error and phase error.

$$\Delta r_{ij}(t) = \Delta r_i(t) - \Delta r_j(t), \qquad \tau_{ij}(t) = \frac{\Delta r_{ij}(t)}{c} \tag{3.2}$$

This error propagation relationship connects the transmitter antenna model, source attitude, near-field line-of-sight geometry, and VLBI baseline observables, and forms the basis for evaluating the influence of artificial-source phase-centre errors in this study.

In the three model layers described above, the source position and attitude models serve as common inputs. For Genesis, the simulation adopts a circular orbit approximation, nadir-pointing attitude, and yaw-steering model to describe the rapidly varying position, line-of-sight direction, and transmitting antenna pointing of the near-Earth artificial source. For NovaMoon, the simulation adopts a geometric model combining a fixed point on the lunar surface with the lunar motion around the Earth, and uses an Earth-pointing attitude to describe the pointing relationship between the lunar surface transmitter and the Earth. The two types of artificial sources are calculated under the same ground station network, frequency settings, target spectral flux density, and loss assumptions, so that the comparison focuses on the differences in source geometric scale, motion characteristics, and attitude model.

In summary, the Python simulation framework connects the artificial-source position and attitude model, dual-station common-view geometry, reverse link budget, and phase-centre error propagation within a unified computational procedure. The near-field geometry model provides the observable time windows, the link budget model evaluates the transmission conditions required to achieve the target received signal strength, and the phase-centre error model converts transmitter antenna errors into VLBI baseline delay and phase errors. These results together form the physical basis for the subsequent result analysis and VieSched++ scheduling study.

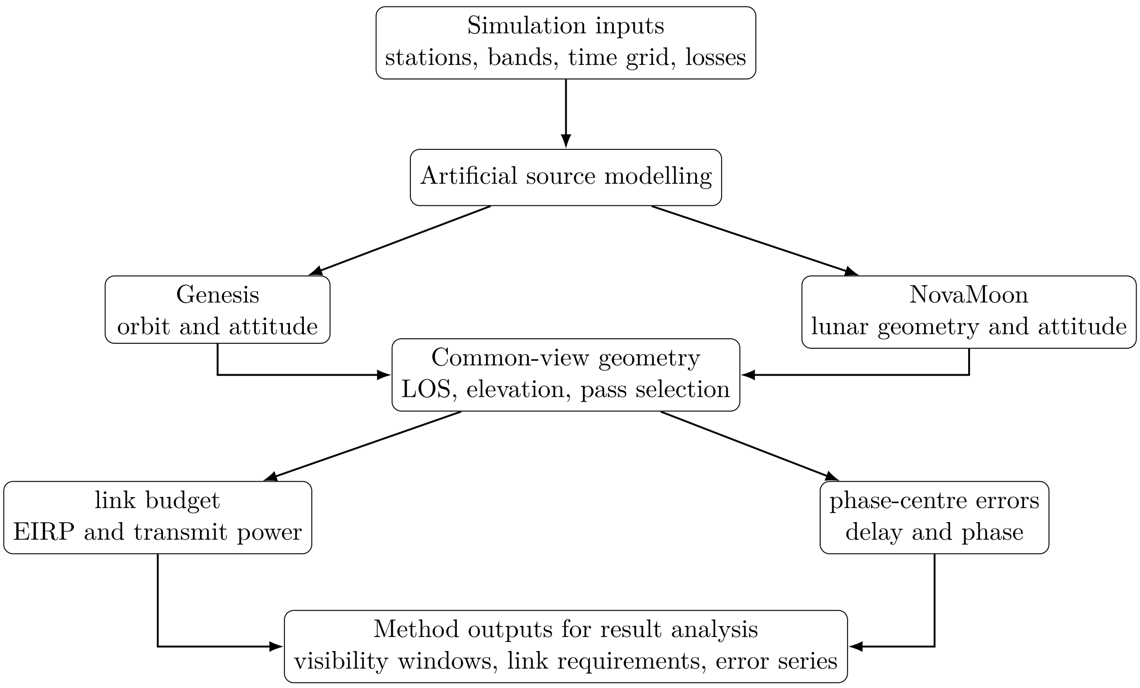

Figure 3.1: Overall workflow of the Python simulation method.

3.2 Simulation Inputs and Basic Assumptions

This section defines the common input parameters and basic assumptions used in the Python simulation for the two artificial source types, Genesis and NovaMoon.

These inputs serve as the common basis for the subsequent geometric visibility, link budget, and phase-centre error propagation models. By evaluating the two artificial sources under the same ground station network, frequency configuration, target received signal strength, and propagation loss assumptions, the subsequent comparison can focus on the differences in geometric scale, motion characteristics, and attitude models of the sources themselves.

Within the simulation framework of this study, Genesis is modeled as a near-Earth orbit artificial transmitter source with rapidly varying observation geometry, while NovaMoon is modeled as a lunar surface artificial transmitter source with a much longer propagation distance and relatively slow line-of-sight variation. Although the two sources adopt different position and attitude models, the subsequent common-view determination, link budget calculation, and phase-centre error propagation are all performed under the same set of baseline assumptions. This treatment avoids introducing additional differences caused by variations in ground station selection, frequency settings, or receiving requirements.

Table 3.1: Common simulation settings and source-specific assumptions.

Item	**Genesis**	**NovaMoon**
Simulation duration	24 h	24 h
Time step	1 s	60 s
Frequency bands	S-band and X-band	S-band and X-band
Centre frequencies	2.26 GHz, 8.59 GHz	2.26 GHz, 8.59 GHz
Observation bandwidth	32 MHz	32 MHz
Target SEFD	10 Jy	10 Jy
Minimum elevation angle	5 deg	5 deg

Table 3.1 summarizes the common settings and source-specific assumptions used in the simulations of the two artificial sources. Among them, the frequency, bandwidth, target spectral flux density, and minimum elevation constraint define identical observation requirements, while the motion and attitude models reflect the primary physical differences between Genesis and NovaMoon. The following subsections further describe how the ground station network, frequency and signal requirements, temporal sampling and elevation constraints, and propagation loss models are incorporated into the complete observability evaluation framework.

3.2.1 Ground Station Network

This study adopts a baseline configuration using Onsala as the reference station. Onsala forms four independent baselines with Wettzell, Sheshan, GGAO, and Hartebeesthoek, respectively, to evaluate the observability of artificial sources under different geographic distributions and baseline geometries. The purpose of selecting this ground station network is not to construct a complete operational VGOS network, but rather to obtain a representative spatial distribution. The selected stations are distributed across Europe, Asia, North America, and Africa, providing observation geometries with different longitude ranges, continental locations, and baseline orientations.

Such geographic distribution is particularly important for artificial-source VLBI simulations. For conventional far-field AGN sources, the incoming wavefront direction received at different stations can usually be approximated as the same celestial direction. However, for finite-distance artificial transmitter sources such as Genesis and NovaMoon, different stations may correspond to different line-of-sight directions, propagation distances, elevation angles, and atmospheric propagation paths at the same epoch. Therefore, a geographically distributed station configuration can more effectively evaluate the sensitivity of artificial-source observability to baseline geometry and regional observation conditions. Table 3.2 lists the ground station network parameters used in the Python simulation of this study.

Table 3.2: Ground station network used in the Python simulation.

Station	**Latitude (deg)**	**Longitude (deg)**	**Height (m)**	**Diameter (m)**	**SEFD S/X (Jy)**
Onsala	57.3936	11.9197	53.3	13.2	2900 / 2000
Wettzell	49.1439	12.8777	672.5	13.2	2500 / 2500
Sheshan	31.0996	121.1993	28.1	13.0	3000 / 3000
GGAO	39.0220	-76.8273	18.5	12.0	2100 / 2800
Hartebeesthoek	-25.8877	27.6860	1418.2	13.2	3100 / 2600

In this simulation, the baseline rather than the individual station is used as the fundamental analysis unit. For any baseline formed by Onsala and a target station i, an epoch is used for subsequent link budget and phase-centre error propagation analysis only when both stations simultaneously satisfy the minimum elevation constraint. The link budget must also simultaneously consider the receiving conditions at both ends of the baseline, while the phase-centre error analysis compares the projection difference of the same transmitter error along two different line-of-sight directions. Therefore, the ground station network not only defines the locations of the observation points, but also directly determines the basis for the calculation of common-view windows, propagation distances, atmospheric losses, and differential errors.

Each ground station in the simulation is characterized by its ECEF coordinates, geodetic latitude and longitude, altitude, antenna diameter, and SEFD values at different frequency bands. The ECEF coordinates are used to calculate the line-of-sight vectors, propagation distances, and elevation angles between the source and the station. The geodetic latitude, longitude, and altitude are used in the ITU-R atmospheric propagation model, while the antenna diameter and SEFD characterize the fundamental scale and sensitivity of the receiving system.

For an arbitrary station i, the fundamental geometric relationship between the station and the artificial source is determined by the station ECEF position $\mathbf{r}_{i,E}$ and the source ECEF position $\mathbf{r}_{s,E}(t)$. The line-of-sight vector and slant range are defined as

$$\boldsymbol{\rho}_i(t) = \mathbf{r}_{s,E}(t) - \mathbf{r}_{i,E}, \qquad d_i(t) = \|\boldsymbol{\rho}_i(t)\| \tag{3.3}$$

This geometric relationship serves as the starting point for all subsequent baseline calculations. The line-of-sight vector is transformed into the local ENU coordinate system to obtain the elevation angle used for common-view determination, while the slant range $d_i(t)$ enters the propagation-distance term in the link budget. The projection difference of the same transmitter phase-centre error along different $\boldsymbol{\rho}_i(t)$ directions forms the differential path error on the baseline. Therefore, the ground station network and baseline configuration are not only simulation input conditions, but also the foundation connecting geometric visibility, link feasibility, and error propagation models.

3.2.2 Frequency Setup and Signal Requirement

The Python simulation in this study is performed in both the S-band and X-band frequency ranges, with centre frequencies set to 2.2600 GHz and 8.5900 GHz, respectively. The observation bandwidth is uniformly set to 32 MHz. For the link budget, the frequency determines the atmospheric propagation loss conditions and affects the estimation of the required transmit power at different frequency bands. For the phase-centre error analysis, the wavelength corresponding to each frequency determines how the same differential path error appears in the phase observation.

In this study, the target spectral flux density required at the ground receiving stations is set to 10 Jy. This value serves as the receiving-side constraint in the reverse link budget and is used to derive the required EIRP and transmit power from the desired received signal strength. Starting from the prescribed receiving signal requirement, the simulation evaluates the transmission conditions that the artificial source must satisfy under different source–station geometric configurations.

$$S_{\mathrm{req}} = 10\ \mathrm{Jy} = 10 \times 10^{-26}\ \mathrm{W\,m^{-2}\,Hz^{-1}} \tag{3.4}$$

Here, S_{req} denotes the target spectral flux density used in the subsequent link budget calculations. For each common-view epoch, the simulation separately calculates the propagation distance, off-boresight angle, and propagation loss from the artificial source to the two stations of the baseline, while using S_{req} as the common receiving requirement for both stations. Since the geometric conditions of the two stations are generally different, the corresponding transmission requirements at the same epoch may also differ. The final baseline-level transmission requirement is therefore determined by the more stringent receiving-side constraint.

The frequency parameters are also used to convert path errors into phase errors.

The differential path error caused by the transmitter PCO/PCV is first represented as a path-length quantity and is then converted into phase variation at different frequency bands. Therefore, the S-band and X-band correspond not only to different link budget conditions, but also to different sensitivities to phase error. The same path error produces a larger phase variation at the shorter wavelength of the X-band, making the frequency setup a key input in the phase-centre error propagation model.

$$\phi_{\mathrm{err},b}(t) = 360^\circ \frac{\Delta r(t)}{\lambda_b}, \qquad b \in \{\mathrm{S}, \mathrm{X}\} \tag{3.5}$$

where $\Delta r(t)$ denotes the differential path error between the two ends of the baseline caused by the transmitter phase-centre error, and λ_b is the wavelength corresponding to frequency band b. This relationship shows that the frequency setup not only determines the propagation conditions in the link budget, but also determines the extent to which path errors are amplified at different observation frequency bands.

Therefore, the frequency, bandwidth, and target spectral flux density defined in this subsection together establish the signal observation requirements for the subsequent models. The frequency connects the atmospheric propagation model and the phase error conversion, the bandwidth is used to convert the spectral-density-based transmission requirement into total EIRP and transmit power, and the target spectral flux density provides the receiving-side signal requirement that the artificial source must satisfy. These parameters provide a unified frequency-band basis for the subsequent reverse link budget and phase-centre error analysis.

3.2.3 Time Sampling and Elevation Constraint

A simulation duration of 24 h is adopted for both Genesis and NovaMoon, while different temporal sampling intervals are used for the two artificial source types. Genesis is a near-Earth orbit artificial source whose observation geometry relative to the ground stations changes rapidly over short time scales, and therefore a time step of 1 s is adopted. NovaMoon is located on the lunar surface, and its geocentric direction variation is mainly governed by the lunar motion around the Earth, which changes relatively slowly over a one-day interval. Therefore, a time step of 60 s is adopted. This temporal sampling configuration reflects the different motion time scales of the two artificial sources. For an arbitrary artificial source, Each sampling epoch corresponds to a complete geometric calculation, including the source position and attitude, the line-of-sight direction between the source and each ground station, the slant range, and the elevation angle.

The elevation constraint is used to define the basic observation visibility of the artificial source at the ground stations. A uniform minimum elevation threshold of $e_{\min} = 5^\circ$ is adopted in this study. For any baseline formed by Onsala and a target station i, only sampling epochs satisfying the dual-station common-view condition are used for the subsequent link budget and error propagation analysis. After the elevation filtering process, consecutive sampling epochs satisfying the condition are grouped into common-view passes. Each pass therefore represents a continuous dual-station observation opportunity and serves as the fundamental time window for the subsequent calculations.

The minimum elevation threshold is also directly connected to the atmospheric propagation loss model. The elevation-dependent atmospheric lookup table adopted in this study covers the elevation range from 5° to 90°. Therefore, 5° is not only the minimum geometric visibility requirement, but also the lower boundary for the subsequent atmospheric loss interpolation. In this way, the temporal sampling and elevation constraint together define the valid temporal domain of the model calculations.

3.2.4 Propagation Losses and Atmospheric Model

The propagation losses in the link budget consist of fixed system losses and atmospheric propagation losses. The same fixed-loss assumptions are adopted for both Genesis and NovaMoon, including an implementation loss of 1.5 dB and a polarization loss of 3.0 dB, representing systematic margins in the transmitting and receiving links that are not explicitly modeled by the geometric or atmospheric models.

Unlike the fixed losses, the atmospheric propagation loss is modeled as a quantity varying with station location, station altitude, frequency, and elevation angle. For artificial-source VLBI, the elevation angle of the source relative to different stations changes with time, and the two ends of the same baseline may also correspond to different atmospheric path lengths. Therefore, treating atmospheric loss as a constant would weaken the relationship between geometric conditions and the link budget. In this study, atmospheric attenuation is calculated using ITU-R models.

In the simulation, the total atmospheric attenuation consists of rain attenuation, cloud attenuation, and gaseous absorption, corresponding to the ITU-R P.618, ITU-R P.840, and ITU-R P.676 models, respectively:

$$A_{\text{atm}} = A_{\text{rain}}^{\text{P.618}} + A_{\text{cloud}}^{\text{P.840}} + A_{\text{gas}}^{\text{P.676}} \tag{3.6}$$

where A_{atm} denotes the total atmospheric attenuation, and $A_{\text{rain}}^{\text{P.618}}$, $A_{\text{cloud}}^{\text{P.840}}$, and $A_{\text{gas}}^{\text{P.676}}$ represent the rain attenuation, cloud attenuation, and gaseous absorption attenuation, respectively. The model inputs include the station geodetic latitude, longitude, altitude, link frequency, elevation angle, annual time exceedance probability, and polarization tilt angle. The annual exceedance probability adopted in this study is 1.0, and the polarization tilt angle is set to $-45°$.

To efficiently apply the atmospheric model in the epoch-by-epoch link budget calculation, the simulation adopts an elevation-dependent lookup table method. For each station and frequency band, an atmospheric attenuation table is first precomputed over the elevation range from 5° to 90°. During each subsequent common-view epoch, the atmospheric loss corresponding to the actual elevation angle is obtained through linear interpolation.

$$A_{\mathrm{atm}}(e) = \mathrm{interp}\left(e;\, e_k,\, A_{\mathrm{atm}}(e_k)\right), \qquad 5^\circ \le e \le 90^\circ \tag{3.7}$$

This treatment preserves the primary physical characteristics of atmospheric attenuation variation with elevation angle. Lower elevation angles correspond to longer atmospheric slant paths and therefore generally produce larger propagation attenuation, while higher elevation angles correspond to shorter atmospheric paths and relatively smaller losses. Through the lookup-table interpolation approach, the atmospheric propagation model is connected to the actual geometric conditions at each common-view epoch while avoiding repeated calls to the full ITU-R models for a large number of time samples.

In the link budget calculation, the fixed losses and atmospheric losses are combined into a total loss term. Expressed in dB form, the total environmental loss for a given station, frequency band, and epoch is

$$L_{\mathrm{tot,dB}}(t) = A_{\mathrm{atm}}(t) + L_{\mathrm{impl}} + L_{\mathrm{pol}} \tag{3.8}$$

where L_{impl} denotes the implementation loss and L_{pol} denotes the polarization loss. This total loss is subsequently converted into a linear loss factor and incorporated into the EIRP calculation of the reverse link budget. In this way, the atmospheric propagation model introduces the station geographic environment, frequency configuration, and real-time elevation conditions into the estimation of transmit power requirements, allowing the link budget to reflect not only the propagation distance but also the propagation environment differences across different baselines and observation time windows.

3.3 Genesis Satellite Source Model

In this study, Genesis is modeled as a near-Earth orbit artificial VLBI transmitter source. Unlike conventional AGN sources, Genesis is located at a finite distance and exhibits significant temporal variation relative to the ground stations. Therefore, it cannot be represented as a fixed far-field direction on the celestial sphere, and its position, velocity, propagation distance to each station, and corresponding line-of-sight direction must be calculated at every simulation epoch.

A simplified circular orbit model is adopted to describe the orbital motion of Genesis. The purpose of this approximation is not to perform precise orbital dynamics analysis, but rather to construct a representative near-Earth artificial source motion model under controlled conditions. The circular orbit model preserves the primary characteristics of Genesis, including rapid motion relative to the ground stations, significant elevation variation, and limited common-view windows, while avoiding the introduction of orbital perturbations, attitude maneuvers, or orbit determination errors. This allows the present section to focus on the relationship between artificial-source geometry, attitude pointing, and VLBI observability.

In addition to the orbital position, the attitude model of Genesis is also a key input for the subsequent calculations. The transmitting antenna main axis and phase-centre offset are both defined in the satellite body coordinate system. Therefore, the attitude relationship between the body frame and the Earth-fixed coordinate system must be established. In this study, an attitude model combining nadir-pointing and yaw-steering is adopted, allowing the satellite to maintain Earth-pointing orientation while describing body attitude variation caused by solar constraints through yaw rotation about the nadir direction. This attitude model is subsequently used to determine the antenna boresight direction in the Earth-fixed coordinate system and to transform the PCO/PCV-related quantities into a coordinate framework consistent with the ground-station line-of-sight directions.

Therefore, the Genesis source model consists of both orbital geometry and attitude geometry. The orbital model provides the satellite centroid position and velocity, while the attitude model provides the spatial orientation of the antenna main axis and phase-centre offset. Together, they determine the observation geometry of Genesis relative to each ground station.

3.3.1 Circular Orbit Model

The orbital motion of Genesis is approximated using a circular orbit model. In the simulation, the orbital altitude is set to 6000 km, the orbital inclination is set to 95.5°, and the Earth radius is taken as 6371 km. The orbital radius is determined by the sum of the Earth radius and orbital altitude. Under the circular orbit assumption, the satellite moves within the orbital plane with constant angular velocity, and the orbital phase varies linearly with time. This model provides the position and velocity of Genesis in the inertial coordinate system at every simulation epoch.

$$\mathbf{r}_{\text{orb}}(t) = R_{\text{orb}} \begin{bmatrix} \cos M(t) \\ \sin M(t) \\ 0 \end{bmatrix}, \qquad \mathbf{v}_{\text{orb}}(t) = v_{\text{orb}} \begin{bmatrix} -\sin M(t) \\ \cos M(t) \\ 0 \end{bmatrix} \tag{3.9}$$

where R_{orb} denotes the orbital radius, v_{orb} denotes the circular orbital velocity, and $M(t)$ denotes the orbital phase. In the simulation, the initial phase is set to 180°. The position and velocity vectors within the orbital plane are subsequently rotated into the ECI coordinate system according to the orbital inclination.

Since the ground station coordinates are defined in the ECEF coordinate system, the Earth's rotation must also be considered to transform the Genesis inertial coordinates into the Earth-fixed frame.

$$\mathbf{r}_E(t) = \mathbf{R}_{I\to E}(t)\mathbf{r}_I(t), \qquad \mathbf{R}_{I\to E}(t) = \begin{bmatrix} \cos\theta_E(t) & \sin\theta_E(t) & 0 \\ -\sin\theta_E(t) & \cos\theta_E(t) & 0 \\ 0 & 0 & 1 \end{bmatrix} \tag{3.10}$$

where $\mathbf{r}_I(t)$ and $\mathbf{r}_E(t)$ denote the Genesis position in the ECI and ECEF coordinate systems, respectively, and $\theta_E(t)$ is the rotation angle caused by the Earth's rotation. After this coordinate transformation, the Genesis position can be directly subtracted from the ECEF coordinates of the ground stations to obtain the line-of-sight vectors, slant ranges, and elevation angles corresponding to each station.

The primary role of this circular orbit model in this study is to establish the near-field observation geometry of Genesis, which is calculated epoch by epoch as a three-dimensional spatial point located at finite distance. The subsequent common-view determination, off-boresight angle calculation, link budget analysis, and phase-centre error projection are all based on this near-field geometric description.

3.3.2 Genesis Attitude Model

The orbital model of Genesis provides the position and velocity of the satellite centroid in space, but the orbital state alone is insufficient for the subsequent link budget and phase-centre error analysis. The transmitting antenna boresight and phase-centre offset are both defined in the satellite body coordinate system, while the line-of-sight directions of the ground stations are defined in the ECEF coordinate system. Therefore, the attitude relationship between the satellite body frame and the Earth-fixed coordinate system must be established in order to determine the off-boresight angle of the receiving stations relative to the transmitting antenna main axis and to calculate the projection of the PCO/PCV along different line-of-sight directions.

In this study, nadir-pointing is adopted as the fundamental constraint of the Genesis attitude model, such that the satellite body Z-axis points toward the Earth's center. This configuration allows the platform to maintain Earth-pointing orientation, which is consistent with the basic geometric requirement of a near-Earth artificial source transmitting signals toward ground stations. At each simulation epoch, the satellite ECEF position $\mathbf{r}_E(t)$ is used to define the body Z-axis. The ECEF velocity vector is then projected onto the local plane perpendicular to the Z-axis to construct the body X-axis. This process provides an initial body-frame coordinate system associated with the orbital direction.

$$\hat{\mathbf{z}}_B(t) = -\frac{\mathbf{r}_E(t)}{\|\mathbf{r}_E(t)\|}, \qquad \hat{\mathbf{x}}_{B,0}(t) = \frac{\mathbf{v}_E(t) - [\mathbf{v}_E(t)\cdot\hat{\mathbf{z}}_B(t)]\,\hat{\mathbf{z}}_B(t)}{\|\mathbf{v}_E(t) - [\mathbf{v}_E(t)\cdot\hat{\mathbf{z}}_B(t)]\,\hat{\mathbf{z}}_B(t)\|} \tag{3.11}$$

where $\hat{\mathbf{z}}_B(t)$ denotes the body Z-axis direction in the ECEF coordinate system, and $\hat{\mathbf{x}}_{B,0}(t)$ denotes the initial body X-axis direction before yaw-steering. The initial body Y-axis is determined according to the right-hand coordinate system relationship. This attitude framework ensures that the satellite always maintains nadir-pointing orientation while providing a reference plane for yaw rotation about the nadir axis.

Based on this framework, a yaw-steering model is further adopted to describe the satellite attitude adjustment about the nadir direction. Yaw-steering is a commonly used satellite attitude control strategy whose basic principle is to maintain a specific geometric relationship between the satellite platform and the Sun direction while preserving the Earth-pointing constraint. For satellites equipped with fixed-mounted antennas or solar-related attitude constraints, this model can describe the variation of the body transverse axes within the local horizontal plane with respect to the Sun direction.

The purpose of adopting this model in the present study is to preserve the primary characteristics of Genesis antenna pointing and phase-centre orientation variation caused by attitude changes while maintaining a simplified orbital dynamics framework. The model introduces a solar-direction constraint by projecting the Sun-direction unit vector $\hat{\mathbf{s}}_{sun}(t)$ in the ECEF coordinate system onto the local plane perpendicular to the nadir direction. The projected Sun direction is then used to determine the yaw angle about the body Z-axis, thereby adjusting the directions of the body X- and Y-axes within the local plane.

$$\mathbf{s}_\perp(t) = \hat{\mathbf{s}}_{sun}(t) - \left[\hat{\mathbf{s}}_{sun}(t) \cdot \hat{\mathbf{z}}_B(t)\right] \hat{\mathbf{z}}_B(t), \qquad \hat{\mathbf{s}}_\perp(t) = \frac{\mathbf{s}_\perp(t)}{\|\mathbf{s}_\perp(t)\|} \tag{3.12}$$

The projected Sun direction is decomposed within the initial body X/Y plane:

$$\begin{aligned} s_x(t) &= \hat{\mathbf{s}}_\perp(t) \cdot \hat{\mathbf{x}}_{B,0}(t), \qquad s_y(t) = \hat{\mathbf{s}}_\perp(t) \cdot \hat{\mathbf{y}}_{B,0}(t), \\ \psi(t) &= \operatorname{atan2}\left[-s_x(t), s_y(t)\right] \end{aligned} \tag{3.13}$$

where $\psi(t)$ denotes the yaw-steering angle. According to this yaw angle, the body X- and Y-axes are rotated within the plane perpendicular to the nadir direction:

$$\begin{aligned} \hat{\mathbf{x}}_B(t) &= \cos\psi(t)\hat{\mathbf{x}}_{B,0}(t) + \sin\psi(t)\hat{\mathbf{y}}_{B,0}(t), \\ \hat{\mathbf{y}}_B(t) &= -\sin\psi(t)\hat{\mathbf{x}}_{B,0}(t) + \cos\psi(t)\hat{\mathbf{y}}_{B,0}(t) \end{aligned} \tag{3.14}$$

This yaw-steering attitude model has direct roles in the subsequent calculations. First, the transmitting antenna boresight is defined as a fixed direction in the body coordinate system, and its direction in the ECEF coordinate system is obtained through the attitude transformation. The angle between this direction and the ground-station line-of-sight direction determines the off-boresight gain attenuation in the link budget.

Second, the PCO vector of Genesis is also defined in the body coordinate system, and the attitude model determines its orientation in the Earth-fixed coordinate system, thereby affecting its projection along the line-of-sight directions of different ground stations. Therefore, yaw-steering is not an isolated attitude description, but rather a key model connecting the satellite platform attitude, antenna pointing, link budget, and phase-centre error propagation.

3.3.3 Attitude Representation

After determining the body-axis directions of Genesis, the attitude model must be represented in a coordinate transformation form suitable for subsequent calculations. In this study, a Body-to-ECEF rotation matrix is used to describe the orientation relationship between the satellite body coordinate system and the ECEF coordinate system. This matrix is constructed from the ECEF components of the body X-, Y-, and Z-axes.

$$\mathbf{R}_{B\to E}(t) = \begin{bmatrix}\hat{\mathbf{x}}_B(t) & \hat{\mathbf{y}}_B(t) & \hat{\mathbf{z}}_B(t)\end{bmatrix} \tag{3.15}$$

This rotation matrix serves as the core coordinate interface in the subsequent link budget and error propagation calculations. For an arbitrary vector $\mathbf{a}_B$ defined in the body coordinate system, its representation in the ECEF coordinate system is

$$\mathbf{a}_E(t) = \mathbf{R}_{B\to E}(t)\mathbf{a}_B \tag{3.16}$$

In the link budget analysis, $\mathbf{a}_B$ may represent the transmitting antenna boresight, and the transformed vector $\mathbf{a}_E(t)$ is used to calculate the off-boresight angle between the receiving-station line-of-sight direction and the antenna main axis. In the phase-centre error propagation analysis, $\mathbf{a}_B$ may represent the PCO vector for a specific frequency band, and the transformed ECEF vector is used to calculate the projection of this offset along the line-of-sight directions of different stations. Therefore, $\mathbf{R}_{B\to E}(t)$ directly connects the Genesis attitude model to the subsequent Q1 link budget and Q2 phase-centre error analysis.

In addition to the Body-to-ECEF rotation matrix, the simulation also constructs an Inertial-to-Body rotation matrix to describe the representation of inertial-frame directions in the satellite body coordinate system. This matrix is obtained by combining the Earth-rotation transformation and the Body-to-ECEF transformation:

$$\mathbf{R}_{I\to B}(t) = \mathbf{R}^T_{B\to E}(t)\mathbf{R}_{I\to E}(t) \tag{3.17}$$

where $\mathbf{R}_{I\to E}(t)$ denotes the Earth-rotation matrix from the ECI coordinate system to the ECEF coordinate system. Since the orbital propagation is first defined in the ECI coordinate system, while the ground-station geometry and link calculations are performed in the ECEF coordinate system, this matrix provides a consistent representation of the Genesis attitude between the inertial reference frame and the body coordinate system.

To represent the continuously varying three-dimensional attitude in a compact form, $\mathbf{R}_{I\to B}(t)$ is further converted into a quaternion sequence. Quaternion representation avoids Euler-angle singularities and is suitable for describing continuously varying attitude sequences over time. In the simulation, the sign continuity of adjacent quaternions is maintained to avoid discontinuous jumps caused by the equivalent $\mathbf{q}$ and $-\mathbf{q}$ representations within the time sequence.

Therefore, the attitude representation is not merely an independent output format, but rather the transformation layer between the Genesis source model and the subsequent observation calculations. It converts the body coordinate system obtained from the orbital and yaw-steering models into a unified mathematical representation suitable for antenna pointing, off-boresight gain calculation, PCO projection, and quaternion attitude sequences.

3.4 NovaMoon Source Model

In this study, NovaMoon is modeled as an artificial VLBI transmitter source located on the lunar surface. Unlike the near-Earth Genesis satellite source, the primary geometric characteristics of NovaMoon are determined not by rapid orbital motion around the Earth, but by the Earth–Moon distance scale and the fixed position on the lunar surface. Its line-of-sight direction relative to the ground stations changes more slowly, while the propagation distance is significantly longer. Therefore, the subsequent link budget is more strongly affected by free-space propagation distance and atmospheric path conditions. The purpose of this section is to define the position and attitude models of NovaMoon and to provide the source-side inputs for the subsequent common-view geometry, link budget, and phase-centre error propagation analysis.

Within the overall simulation framework of this chapter, NovaMoon shares the same ground station network, frequency configuration, minimum elevation constraint, common-view determination method, link budget formulation, and phase-centre error propagation framework as Genesis. Therefore, this section focuses on the two characteristics specific to the lunar surface source: the fixed lunar-surface geometry and the Earth-pointing attitude model. The fixed lunar-surface geometry describes how the transmitter source changes its geocentric position through the overall lunar motion, while the Earth-pointing attitude model describes how the transmitting antenna on the lunar surface is oriented relative to the Earth direction. Together, these two models determine the source position, antenna boresight direction, and phase-centre offset orientation of NovaMoon at each simulation epoch.

3.4.1 Lunar Surface Geometry

NovaMoon is treated as a transmitter station fixed on the lunar surface. Therefore, its position is first defined in the Moon-fixed coordinate system rather than being obtained through an independent Earth-orbit propagation as in the Genesis model. Let the latitude and longitude of the lunar station be denoted by ϕ_m and λ_m, respectively, and let the lunar radius be denoted by R_m. The position vector of the station relative to the lunar center can then be expressed using spherical geometry as

$$\mathbf{r}_{\text{site},m} = R_m \begin{bmatrix} \cos\phi_m \cos\lambda_m \\ \cos\phi_m \sin\lambda_m \\ \sin\phi_m \end{bmatrix} \tag{3.18}$$

This vector remains constant in the Moon-fixed coordinate system, indicating that there is no relative motion between NovaMoon and the lunar surface. In the simulation, the motion of the lunar center relative to the Earth is approximated using a circular geocentric orbit. The lunar surface station moves together with the Moon as a whole, and its inertial-frame position is jointly determined by the lunar-center position and the fixed lunar-surface offset:

$$\mathbf{r}_{\text{NM},I}(t) = \mathbf{r}_{\text{Moon},I}(t) + \mathbf{R}_m(t)\mathbf{r}_{\text{site},m} \tag{3.19}$$

where $\mathbf{r}_{\text{NM},I}(t)$ denotes the position of NovaMoon in the ECI coordinate system, $\mathbf{r}_{\text{Moon},I}(t)$ denotes the lunar-center position, and $\mathbf{R}_m(t)$ denotes the rotation matrix transforming the Moon-fixed station offset into the inertial frame. This expression reflects the fundamental characteristic of the NovaMoon model: the source position is not represented as a simple lunar-center point, but rather as the combined result of the Earth–Moon geometry and the fixed lunar-surface location.

3.4.2 NovaMoon Attitude Model

The attitude model of NovaMoon adopts an Earth-pointing assumption, meaning that the transmitting antenna main axis is always directed toward the Earth. This assumption is suitable for the fundamental observation scenario of a lunar-surface artificial transmitter source: the transmitting terminal is located on the lunar surface, while the receiving network is located on the Earth surface, and therefore the antenna reference direction should be related to the direction from the lunar station toward the Earth.

Unlike the yaw-steering attitude model of Genesis, NovaMoon does not require rapid attitude adjustment about the nadir axis as in near-Earth satellites. Its primary attitude constraint is to maintain Earth-pointing orientation.

In the ECEF coordinate system, if the position vector of NovaMoon is denoted by $\mathbf{r}_{s,E}(t)$, then the body Z-axis can be defined as the unit vector pointing from the source toward the Earth's center:

$$\hat{\mathbf{z}}_B(t) = -\frac{\mathbf{r}_{s,E}(t)}{\|\mathbf{r}_{s,E}(t)\|} \tag{3.20}$$

This direction provides the principal constraint of the Earth-pointing attitude model. To construct a complete body coordinate system, the simulation further selects a reference direction and projects it onto the plane perpendicular to $\hat{\mathbf{z}}_B(t)$ in order to define the body X-axis, while the body Y-axis is determined according to the right-hand coordinate system relationship. The resulting body coordinate system forms a Body-to-ECEF attitude matrix which, similarly to the Genesis model, is used for the subsequent coordinate transformation of antenna directions and phase-centre offsets.

The Earth-pointing attitude model has two functions in the subsequent calculations. First, the transmitting antenna boresight is defined as a fixed direction in the body coordinate system, and after attitude transformation its direction in the ECEF coordinate system can be obtained. This direction is then used to calculate the off-boresight angle of the ground stations relative to the antenna main axis. The off-boresight angle enters the antenna gain attenuation term in the link budget.

Second, the PCO vector of NovaMoon is also defined in the source body coordinate system, and the attitude model determines its direction in the ECEF coordinate system, thereby further affecting its projection along the line-of-sight directions of different ground stations. Therefore, the Earth-pointing attitude is not merely an independent geometric assumption, but rather a key model connecting the lunar-surface source position, antenna pointing, link budget, and phase-centre error propagation.

Through the lunar-surface geometry and Earth-pointing attitude definitions described above, NovaMoon is represented as a finite-distance artificial transmitter source that is fixed on the lunar surface and oriented toward the Earth. This model preserves the primary differences between the lunar-surface source and Genesis, including the longer propagation distance, slower line-of-sight variation, and different attitude constraints. The subsequent common-view geometry, reverse link budget, and phase-centre error propagation analyses are all based on the outputs of this source model.

3.5 Common-View Geometry

After the source position and attitude of Genesis and NovaMoon have been determined, the simulation must convert the single-station geometric relationships into baseline-level observable time windows for VLBI observations. For artificial transmitter sources, the line-of-sight direction, slant range, and elevation angle from the source to different ground stations must be calculated separately. Only when the same source simultaneously satisfies the observation conditions at both ends of a baseline during the same epoch can that epoch be used for the subsequent link budget and phase-centre error analysis.

For an arbitrary ground station i, the ECEF line-of-sight vector from the source to the station is defined as

$$\boldsymbol{\rho}_i(t) = \mathbf{r}_{s,E}(t) - \mathbf{r}_{i,E}, \qquad d_i(t) = \|\boldsymbol{\rho}_i(t)\| \tag{3.21}$$

where $\mathbf{r}_{s,E}(t)$ denotes the position of the artificial source in the ECEF coordinate system, $\mathbf{r}_{i,E}$ denotes the ECEF coordinates of station i, and $d_i(t)$ denotes the slant range from the source to the station. The line-of-sight vector is subsequently transformed into the local ENU coordinate system of the station in order to calculate the elevation angle:

$$e_i(t) = \tan^{-1}\left(\frac{\rho_{i,U}(t)}{\sqrt{\rho_{i,E}^2(t) + \rho_{i,N}^2(t)}}\right) \tag{3.22}$$

where $\rho_{i,E}(t)$, $\rho_{i,N}(t)$, and $\rho_{i,U}(t)$ denote the east, north, and up components of the line-of-sight vector in the local coordinate system, respectively. The elevation angle $e_i(t)$ is the fundamental quantity used to determine single-station visibility and also serves as the input for the subsequent atmospheric-loss interpolation.

In this study, Onsala is selected as the reference station and forms baselines with the other ground stations. For a baseline formed by Onsala and station j, the common-view condition is defined such that the elevation angles at both stations simultaneously exceed 5°. This condition converts single-station visibility into baseline observability. Consecutive sampling epochs satisfying common-view are grouped into common-view passes, where each pass represents a continuous dual-station observation opportunity. The subsequent reverse link budget and phase-centre error propagation calculations are performed only within these common-view passes.

Therefore, the common-view geometry model serves as a bridge within the methodology of this study. The source model provides the artificial-source position and attitude at each epoch, while the ground-station model provides the station positions and local coordinate systems. The common-view model then converts these quantities into baseline-level valid observation windows. These windows subsequently serve as the common temporal domain for the link budget and phase-centre error analyses.

3.6 Link Budget and Error Evaluation

After the common-view passes have been determined, this study further evaluates two quantities within these valid dual-station observation windows. The first is the transmission condition required to achieve the target received signal strength, corresponding to the link budget. The second is the influence of transmitter phase-centre errors on VLBI observables, corresponding to phase-centre error propagation. The former reflects the signal accessibility under different source–baseline geometries, while the latter describes how transmitter antenna reference errors propagate into baseline delay and phase observables.

3.6.1 Inverse Link Budget

The link budget describes the signal-strength relationship among the transmitter, propagation path, and receiver. In this study, it is not used to evaluate the received signal strength for a known transmitter power. Instead, an inverse formulation is adopted: given the target spectral flux density required at the ground receiving stations, the required EIRP and transmit power of the artificial source are derived under the current geometric and propagation conditions.

Therefore, the required EIRP and transmit power should be interpreted as feasibility indicators used to compare the link difficulty of different artificial sources, baselines, frequency bands, and common-view windows.

At each common-view epoch, the link budget is primarily controlled by three factors. The first is the slant range between the source and the receiving station. Larger propagation distance requires stronger transmitting capability to achieve the same spectral flux density. The second factor is the propagation and system loss, including ITU-R atmospheric attenuation, implementation loss, and polarization loss. The third factor is the transmitting antenna pointing condition, namely the off-boresight angle between the receiving-station direction and the transmitting antenna boresight. Larger off-boresight angles correspond to lower effective transmitting gain and therefore require higher transmit power. In the simulation, a Gaussian beam approximation is used to describe the off-boresight gain attenuation, which is incorporated into the link budget as a gain correction term.

For an arbitrary receiving station i, the required EIRP spectral density can be expressed as

$$\mathrm{EIRP}_{\mathrm{PSD},i}(t) = \frac{S_{\mathrm{req}}\, 4\pi d_i^2(t)\, L_{\mathrm{tot},i}(t)}{G_{\mathrm{drop},i}(t)} \tag{3.23}$$

where S_{req} denotes the target spectral flux density, $d_i(t)$ denotes the slant range between the artificial source and station i, $L_{\mathrm{tot},i}(t)$ denotes the total loss factor in linear form, and $G_{\mathrm{drop},i}(t)$ denotes the normalized gain attenuation caused by the off-boresight angle. This expression reflects the central relationship of the link budget in this study: the required transmitting capability is jointly determined by geometric distance, propagation environment, and antenna pointing conditions.

For a VLBI baseline, the receiving signal requirements must be simultaneously satisfied at both stations during the same epoch. Therefore, the simulation separately evaluates the link requirements from the artificial source to the two stations of the baseline and adopts the larger EIRP or transmit power as the baseline-level requirement at that epoch. Subsequently, the best-case and worst-case values within each common-view pass are extracted for comparison of the link feasibility of Genesis and NovaMoon under different baselines and frequency bands in the results chapter.

3.6.2 Phase-Centre Error Propagation

For artificial VLBI transmitter sources, the phase-centre error is located at the transmitting terminal rather than the ground receiving terminal. Since the same artificial source is observed from different directions by the two stations of a baseline, the projection of the same transmitter phase-centre error onto the two propagation paths is generally different. VLBI observations are sensitive to the difference between these two projections, namely the baseline differential path error.

This study considers two types of transmitter phase-centre error. PCO represents the fixed offset of the phase centre relative to the nominal reference point and is usually represented as a vector in the body coordinate system. PCV represents the additional path variation caused by changes in the observation direction and is modeled in this study as a simplified direction-dependent term varying with the off-boresight angle. Together, they describe how the geometric errors of the transmitting antenna propagate into the observation path as a function of source attitude and ground-station line-of-sight direction.

For a PCO vector $\mathbf{a}_B$ corresponding to a specific frequency band, the vector is first transformed into the ECEF coordinate system through the source attitude matrix and then projected onto the unit line-of-sight direction from the source toward station i:

$$\Delta r_{\mathrm{PCO},i}(t) = \hat{\boldsymbol{\rho}}_i(t) \cdot [\mathbf{R}_{B\to E}(t)\mathbf{a}_B] \tag{3.24}$$

where $\hat{\boldsymbol{\rho}}_i(t)$ denotes the unit line-of-sight vector from the artificial source toward station i, and $\mathbf{R}_{B\to E}(t)$ denotes the rotation matrix from the source body coordinate system to the ECEF coordinate system. This expression shows that the influence of the phase-centre error depends not only on the magnitude of the PCO itself, but also on the source attitude and the observation direction of the station relative to the transmitter source.

At each common-view epoch, the simulation separately evaluates the PCO and

PCV path contributions at the two ends of the baseline and defines the difference between the two contributions as the differential path error $\Delta r_{ij}(t)$ of the baseline. This differential path error is further converted into delay error and phase error:

$$\tau_{ij}(t) = \frac{\Delta r_{ij}(t)}{c}, \qquad \phi_{ij,b}(t) = 360^\circ \frac{\Delta r_{ij}(t)}{\lambda_b} \tag{3.25}$$

where $\tau_{ij}(t)$ denotes the baseline delay error, $\phi_{ij,b}(t)$ denotes the phase error at frequency band b, and λ_b denotes the wavelength corresponding to that frequency band. The same path error produces larger phase variation at shorter wavelengths, making the X-band more sensitive to phase-centre errors. By evaluating these quantities within the common-view passes, the influence of transmitter antenna errors on VLBI observations can be assessed for different artificial sources, baselines, and frequency bands.

4

VieSched++ Scheduling Method

This chapter describes the scheduling strategy that we used. The focus is the design of the observing schedules rather than a general introduction to the VieSched++ software. VieSched++ was used as the scheduling tool to implement a controlled set of observing plans involving the Genesis satellite target, the NovaMoon target, and conventional AGN reference sources. The purpose of the schedule design was to test how different source combinations and different station-network scales affect scan distribution, station participation, baseline coverage, and the balance between artificial-source observations and conventional reference-source observations.

Seven observing plans were considered:

- Genesis-5;
- NovaMoon-5;
- Genesis-16;
- NovaMoon-16;
- AGN-16;
- Genesis+NovaMoon-16;
- Genesis+NovaMoon+AGN-16.

The suffixes "5" and "16" indicate the number of stations that be used in the corresponding schedule. The five-station schedules use a basic VGOS subnetwork, while the sixteen-station schedules use the full selected VGOS network in this thesis. Therefore, the notation does not refer to the number of sources, frequency bands, or observing sessions, but specifically to the number of participating stations.

The seven plans define the methodological structure of the scheduling experiment. The Genesis-5 and NovaMoon-5 schedules are used as basic-network cases to evaluate whether each artificial source can be scheduled within a limited station network.

The Genesis-16 and NovaMoon-16 schedules test how the observation opportunities change when the station network is expanded. The Genesis+NovaMoon-16 schedule investigates the joint scheduling of the two artificial sources without AGN support. Finally, the Genesis+NovaMoon+AGN-16 schedule evaluates whether artificial-source observations can still be retained when conventional AGN sources are included in a more complete VLBI observing plan.

In the available VieSched++ installation, Genesis was configured through a satellite TLE input path. NovaMoon was treated as a non-standard lunar target in the scheduling design. Since the current VieSched++ workflow is mainly designed for conventional radio sources and satellite-type targets, the NovaMoon-related schedule should be interpreted as an approximate scheduling experiment for a lunar artificial transmitter rather than a fully operational lunar-station model.

4.1 Role of VieSched++

VieSched++ was used as the scheduling engine for converting the observing concepts into feasible VLBI schedules. Its role was to combine station catalogues, source catalogues, observing-mode settings, satellite or lunar target information, visibility limits, scan-duration settings, and scheduling weights. The resulting schedules were then exported for further inspection and comparison with Python.

In this workflow, VieSched++ is not the object of study itself. It is the implementation environment used to realise the observing-plan set. The scientific focus is how the schedule structure changes when AGN reference sources are combined with Genesis or NovaMoon, when Genesis and NovaMoon are scheduled together, and when each special target is scheduled alone.

4.2 Design of the Observing Plans

The observing plans were designed to compare the effects of source type and station network size on the scheduling performance of artificial-source VLBI. Two artificial sources were considered: Genesis, representing a near-Earth moving transmitter, and NovaMoon, representing a lunar-distance artificial transmitter. In addition, AGN sources were included to represent conventional geodetic VLBI reference sources in both AGN-only and mixed-source scheduling cases.

The seven observing plans are listed in Table 4.1. They are divided according to station-network size and source composition. The first group consists of the five-station single-source schedules, namely Genesis-5 and NovaMoon-5. These schedules are used to test the basic feasibility of scheduling each artificial source with a limited station network. Since only five stations are available, these plans are expected to be more sensitive to target visibility and baseline geometry.

The second group consists of the sixteen-station single-source schedules, Genesis-

16 and NovaMoon-16. These schedules use the same artificial sources as the first group but with an expanded station network. Their purpose is to examine whether increasing the number of stations improves scan numbers, station participation, baseline coverage, and multi-station observing opportunities.

The third group consists of the sixteen-station multi-source schedules. The Genesis+NovaMoon-16 schedule includes both artificial sources but no AGN sources. It is used to test whether the two artificial targets can be scheduled together and how the observing time is distributed between them. The Genesis+NovaMoon+AGN-16 schedule further includes conventional AGN sources. This final plan represents a mixed observing strategy in which artificial sources are embedded into a more conventional VLBI schedule.

Table 4.1: Conceptual structure of the VieSched++ observing-plan design.

Plan	Target composition	Main purpose
G-5	Genesis	Test Genesis scheduling in a five-station network.
N-5	NovaMoon	Test NovaMoon scheduling in a five-station network.
G-16	Genesis	Evaluate the effect of network expansion for Genesis.
N-16	NovaMoon	Evaluate the effect of network expansion for NovaMoon.
A-16	AGN	Evaluate the sixteen-station AGN reference-source schedule.
G+N-16	Genesis and NovaMoon	Test joint artificial-source scheduling.
G+N+A-16	Genesis, NovaMoon, AGN	Test artificial sources in a mixed VLBI schedule.

Note: G denotes Genesis, N denotes NovaMoon, A denotes AGN, and the number indicates the station-network size.

This design allows the effects of source type, station-network expansion, and source combination to be compared. First, Genesis-5 and NovaMoon-5 are compared to identify the difference between the two artificial sources in a limited network. Second, the five-station and sixteen-station schedules are compared to evaluate the influence of station-network expansion. Third, the single-source, dual-artificial-source, and AGN-mixed schedules are compared to determine how source combination changes the scheduling structure.

4.3 Stations, Sources, and Equipment Configuration

The station and equipment configuration was kept as consistent as possible across the schedule set so that differences in the final results could mainly be attributed to target selection. The station network determines which baselines can observe a target at a given time, while the equipment and observing mode define the technical compatibility and observation setup.

For schedules containing AGNs, the AGN source list was selected from the VieSched++ radio-source catalogue. These sources provide broad sky coverage and support the stability of geodetic VLBI scheduling. In AGN-containing schedules, AGN sources provide the reference-source framework, while artificial-source observations are added where applicable.

Genesis was configured as a moving satellite target. In the available VieSched++ settings, the satellite path points to `E:/VieSchedInput/Genesis_TARGET.tle`, indicating that its position was derived from orbital information rather than from a fixed celestial-source catalogue. Its visibility depends on station location, observing time, elevation limits, and the orbital elements in the TLE file.

NovaMoon was treated as a non-standard lunar target in the scheduling design. Its motion and visibility differ from both fixed AGNs and an artificial satellite such as Genesis. This makes NovaMoon useful for testing how VieSched++ handles schedules where the observing opportunity is governed by a lunar target rather than by a fixed celestial source list.

4.4 Configuration of the Schedules

VieSched++ observation plans are implemented through a unified scheduling framework. The five-station scheduling plan is implemented using a selected subset of the VGOS subnetwork, while the sixteen-station scheduling plan uses the complete selected VGOS network. Scheduling plans containing only Genesis and those containing only NovaMoon are used, respectively, to evaluate the scheduling behavior for each artificial source.

For observation plans containing AGN sources, standard radio source catalogs and flux information were incorporated into the VieSched++ input configuration. The AGN-only observation plan uses the same 16-station network as the other 16-station observation plans, but does not include artificial source inputs. This allows it to be compared with both artificial source and mixed-source observation plans, while retaining the characteristics of an AGN-based VLBI observation plan as a standard reference source.

The Genesis+NovaMoon observation plan is implemented by incorporating both artificial sources into the same observation window. This configuration is used to examine whether the two target artificial sources can be jointly scheduled and how available observation time is allocated between them. Since no AGN sources are included in this case, this observation plan directly reflects the competitive and complementary relationship between the two target artificial sources.

The Genesis+NovaMoon+AGN observation plan incorporates these two artificial sources alongside a traditional AGN source. This configuration is used to examine how observations of artificial sources can be preserved when they are embedded within AGN-based VLBI observation plans. Therefore, by comparing this plan with corresponding single-source, dual-artificial-source, and pure AGN plans, it provides a controlled basis for evaluating the impact of source composition on the final VieSched++ plan structure.

4.5 Scheduling Constraints and Weights

The scheduling design was controlled by constraints and weights. Constraints define which scans are allowed, while weights define which allowed scans are preferred. The most important constraints include minimum elevation, scan duration, source or target repeat interval, station slewing time, and station-baseline participation.

For AGN observations, the constraints help maintain a useful geodetic schedule by avoiding poor low-elevation observations and excessive repetition of the same source. For Genesis and NovaMoon, visibility constraints are more critical because the target positions change with time and may not be observable from all stations simultaneously.

In AGN-containing mixed schedules, the weights must balance reference-source geometry against artificial-source observation density. In the Genesis + NovaMoon schedule, the weights instead balance two special targets against each other. This is an important methodological difference: the question is no longer how much AGN geometry can be preserved, but how observing time is distributed between Genesis and NovaMoon.

In the target-only schedules, the weighting problem is simpler, but the geometric limitation is stronger. Since only one target is available, scan timing is mainly determined by visibility windows and station participation. These schedules are useful for identifying the maximum practical observing opportunity for each individual target.

4.6 VieSched++ Output Metrics

The VieSched++ output was evaluated using metrics that describe schedule size, target composition, station participation, baseline distribution, and temporal coverage. The total number of scans and observations provides a first measure of schedule productivity, but these values alone are not sufficient. A schedule must also be assessed by how the observations are distributed between targets and across the station network.

For AGN-containing schedules, the target composition is evaluated using the ratio between AGN observations and artificial-source observations where applicable. For the Genesis + NovaMoon schedule, the key metric is the ratio between Genesis and NovaMoon observations. For the target-only schedules, the key metrics are the continuity of target coverage, the number of participating stations, and the number of useful baselines.

The comparison therefore used the following categories:

- schedule size: number of scans, number of observations, and session duration;
- target composition: number and percentage of AGN, Genesis, and NovaMoon scans;
- network participation: number of stations per scan and observations per station;
- baseline distribution: number of observations per baseline;
- temporal distribution: scan spacing, idle time, and target visibility windows;
- geometric behaviour: AGN sky coverage and target-track coverage for Genesis and NovaMoon.

4.7 Comparison with Python Results

Python was used as an independent post-processing environment for the schedules generated by VieSched++. After the schedules were exported, Python scripts were used to classify scans by target type, count observations, summarise station and baseline participation, and compare the observing-plan set using the same definitions.

For AGN-containing schedules, Python was used to separate AGN observations from artificial-source observations and calculate their relative contributions where applicable. For Genesis + NovaMoon, Python was used to determine how the session was divided between the two special targets. For Genesis-only and NovaMoon-only schedules, Python verified that the schedule contained only the intended target and summarised its observing opportunities.

Overall, the scheduling method used in this thesis can be summarised as a two-stage workflow. VieSched++ generated feasible VLBI schedules for the defined observing-plan set. Python then quantified and compared the resulting schedules in terms of target composition, station participation, baseline distribution, and temporal coverage. This workflow makes it possible to evaluate not only whether Genesis and NovaMoon can be scheduled, but also how their inclusion changes the structure of VLBI observing plans.

5

Results and Discussion

5.1 Python Simulation Results for Genesis

This section presents the results for the Genesis. The analysis includes the common-view visibility, the link-budget requirements, and the phase-centre related delay and phase errors. The reference station is Onsala, and the simulated baselines are formed between Onsala and Wettzell, Sheshan, GGAO, and Hartebeesthoek.

The Genesis case is strongly affected by the fast apparent motion of the Earth-orbiting transmitter. The common-view windows are therefore separated into short passes, and the link-budget and phase-error quantities vary during each pass. The Q1 results show that the required transmit power is small for all baselines under the assumed target signal level, but the required EIRP increases for higher frequency bands and for less favourable viewing geometry. The Onsala–Wettzell baseline has the longest total common-view duration (20546 s) and the lowest required power. The Onsala–Hartebeesthoek baseline has only two common-view passes and the shortest total common-view time (1611 s), which makes it less useful in this scenario. The Onsala–Sheshan and Onsala–GGAO baselines have intermediate visibility, with total common-view durations of 6699 s and 10100 s, respectively.

The link-budget output indicates that the worst-case EIRP is largest for Onsala–Sheshan in the highest X-band channel. In this case the required EIRP is 0.1095 W, corresponding to a transmit power of 0.0042 W after the assumed antenna gain. By comparison, the Onsala–GGAO worst-case EIRP in the same band is 0.0570 W. This means that GGAO is not the most demanding baseline. Signal feasibility alone would therefore not identify GGAO as the most problematic case.

The Q2 results show a different behaviour. The largest phase-centre related delay and phase errors occur for the Onsala–GGAO baseline. The maximum total delay error is 443.80 ps for Onsala–GGAO, compared with 280.39 ps for Onsala–Sheshan. The corresponding maximum phase error in the highest X-band channel reaches 1525.77° for Onsala–GGAO. This is larger than the value for Onsala–Sheshan (963.98°), even though the ordinary baseline length and projected baseline are smaller for GGAO.

genesis q1 output table

```
=========== Topic 2 (Genesis) Q1 Results (Final Lightweight Version) ============
Boresight Gain: 14.15 dBi (theta_fwhm = 61.70 deg)
Atmospheric model: P.618 elevation LUT (5.0-90.0 deg, step=2.0 deg)
--------------------------------------------------------------------------------

Baseline: Onsala - Wettzell
Number of common-view passes: 6
Total common-view duration: 20546 seconds.
Frequency Band  | EIRP_best (W)  | Pt_best (W)  | EIRP_worst (W)  | Pt_worst (W)
--------------------------------------------------------------------------------
S-band          | 0.0046         | 0.0002       | 0.0261          | 0.0010
C-band          | 0.0046         | 0.0002       | 0.0281          | 0.0011
X-band-low      | 0.0047         | 0.0002       | 0.0342          | 0.0013
X-band-high     | 0.0047         | 0.0002       | 0.0390          | 0.0015
--------------------------------------------------------------------------------

Baseline: Onsala - Sheshan
Number of common-view passes: 5
Total common-view duration: 6699 seconds.
Frequency Band  | EIRP_best (W)  | Pt_best (W)  | EIRP_worst (W)  | Pt_worst (W)
--------------------------------------------------------------------------------
S-band          | 0.0139         | 0.0005       | 0.0282          | 0.0011
C-band          | 0.0143         | 0.0006       | 0.0370          | 0.0014
X-band-low      | 0.0157         | 0.0006       | 0.0720          | 0.0028
X-band-high     | 0.0166         | 0.0006       | 0.1095          | 0.0042
--------------------------------------------------------------------------------

Baseline: Onsala - GGAO
Number of common-view passes: 5
Total common-view duration: 10100 seconds.
Frequency Band  | EIRP_best (W)  | Pt_best (W)  | EIRP_worst (W)  | Pt_worst (W)
--------------------------------------------------------------------------------
S-band          | 0.0103         | 0.0004       | 0.0268          | 0.0010
C-band          | 0.0105         | 0.0004       | 0.0310          | 0.0012
X-band-low      | 0.0108         | 0.0004       | 0.0448          | 0.0017
X-band-high     | 0.0111         | 0.0004       | 0.0570          | 0.0022
--------------------------------------------------------------------------------

Baseline: Onsala - Hartebeesthoek
Number of common-view passes: 2
Total common-view duration: 1611 seconds.
Frequency Band  | EIRP_best (W)  | Pt_best (W)  | EIRP_worst (W)  | Pt_worst (W)
--------------------------------------------------------------------------------
S-band          | 0.0172         | 0.0007       | 0.0262          | 0.0010
C-band          | 0.0177         | 0.0007       | 0.0294          | 0.0011
X-band-low      | 0.0192         | 0.0007       | 0.0409          | 0.0016
X-band-high     | 0.0202         | 0.0008       | 0.0502          | 0.0019
--------------------------------------------------------------------------------
================================================================================
```

Figure 5.1: Python Q1 link-budget output for the Genesis case.

genesis q2 output table

```
=========== Topic 2 (Genesis) Q2 Results (Final Lightweight Version) ============

Baseline: Onsala - Wettzell
Max Baseline PCO Delay:   130.62 ps
Max Baseline PCV Delay:   1.07 ps
Max Total Delay Error:    129.55 ps
Max Phase Error (S-band):     149.24 deg
Max Phase Error (C-band):     252.78 deg
Max Phase Error (X-band-low):     382.44 deg
Max Phase Error (X-band-high):     445.40 deg
------------------------------------------------------------------

Baseline: Onsala - Sheshan
Max Baseline PCO Delay:   281.69 ps
Max Baseline PCV Delay:   2.03 ps
Max Total Delay Error:    280.39 ps
Max Phase Error (S-band):     323.01 deg
Max Phase Error (C-band):     547.09 deg
Max Phase Error (X-band-low):     827.71 deg
Max Phase Error (X-band-high):     963.98 deg
------------------------------------------------------------------

Baseline: Onsala - GGAO
Max Baseline PCO Delay:   446.95 ps
Max Baseline PCV Delay:   3.29 ps
Max Total Delay Error:    443.80 ps
Max Phase Error (S-band):     511.25 deg
Max Phase Error (C-band):     865.93 deg
Max Phase Error (X-band-low):     1310.08 deg
Max Phase Error (X-band-high):     1525.77 deg
------------------------------------------------------------------

Baseline: Onsala - Hartebeesthoek
Max Baseline PCO Delay:   268.03 ps
Max Baseline PCV Delay:   1.40 ps
Max Total Delay Error:    267.10 ps
Max Phase Error (S-band):     307.70 deg
Max Phase Error (C-band):     521.16 deg
Max Phase Error (X-band-low):     788.48 deg
Max Phase Error (X-band-high):     918.29 deg
------------------------------------------------------------------
==================================================================
```

Figure 5.2: Python Q2 phase-centre error output for the Genesis case.

To understand this result, the ordinary projected baseline length $|\mathbf{B} \cdot \mathbf{s}|$ was compared for the Onsala–Sheshan and Onsala–GGAO baselines. The ECEF baseline length is about 7648 km for Onsala–Sheshan and 6130 km for Onsala–GGAO. The projected baseline is also not larger for GGAO. During common-view windows, the maximum projected baseline is about 5438 km for Sheshan and 4813 km for GGAO. The corresponding mean projected baselines are about 3128 km and 2130 km, respectively.

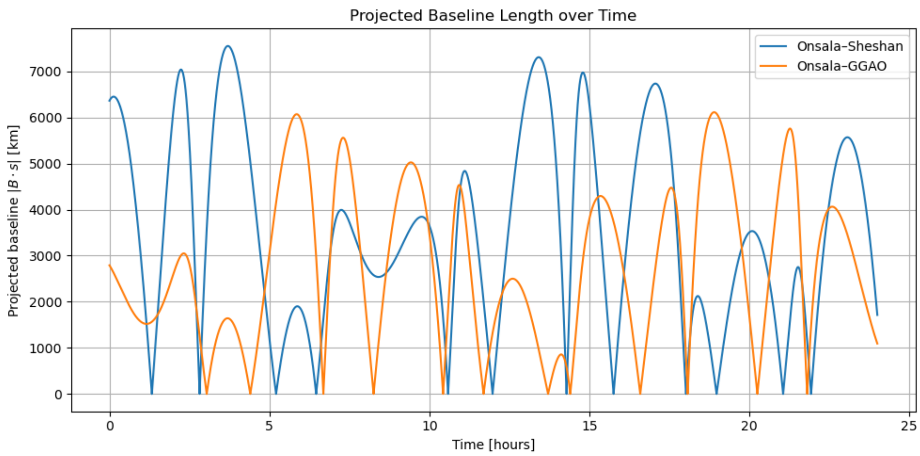

Figure 5.3: Projected baseline length over the full simulated day for Onsala–Sheshan and Onsala–GGAO.

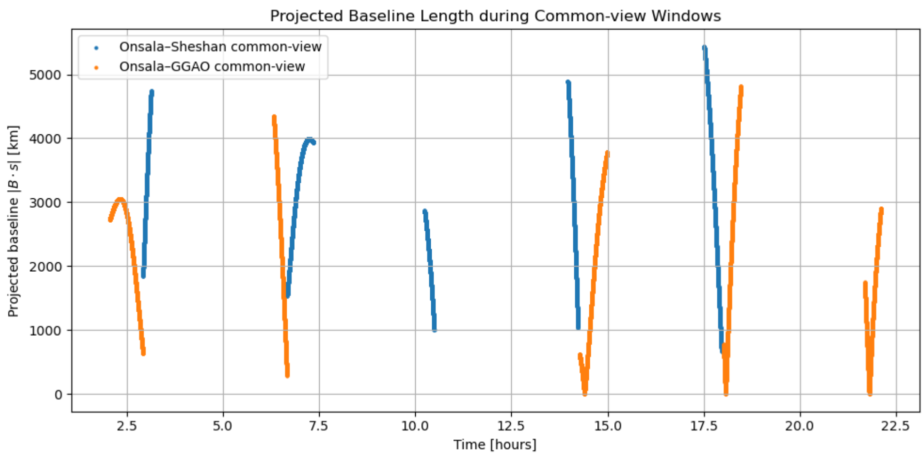

Figure 5.4: Projected baseline length during common-view windows for Onsala–Sheshan and Onsala–GGAO.

These results show that the larger GGAO phase-centre error cannot be explained by the ordinary baseline projection. The dominant effect is instead related to the differential antenna viewing geometry. The two stations in the Onsala–GGAO baseline view the satellite antenna from more different off-boresight directions than in the Onsala–Sheshan case. The maximum off-boresight angle difference is 16.02° for

GGAO and 8.80° for Sheshan, while the mean values are 4.36° and 2.57°, respectively.

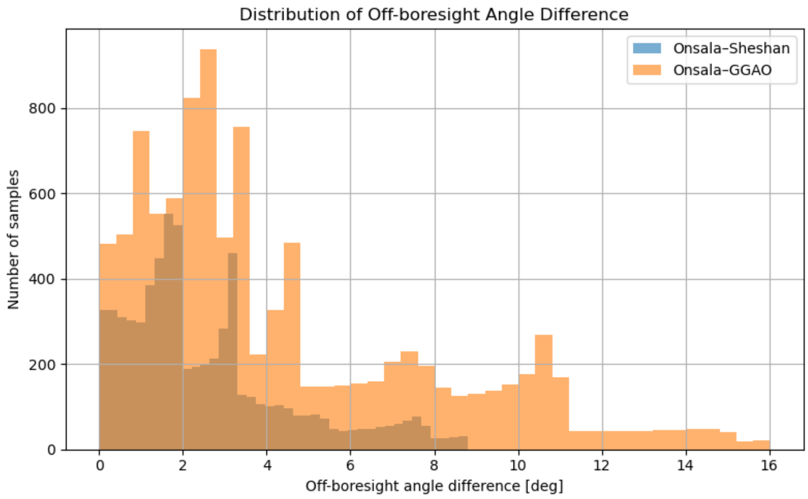

Figure 5.5: Distribution of the off-boresight angle difference for Onsala–Sheshan and Onsala–GGAO.

This differential viewing geometry directly affects the projected PCO and PCV terms. The maximum differential PCO path is 84.51 mm for Onsala–Sheshan and 134.08 mm for Onsala–GGAO. The ratio is about 1.59, which is consistent with the ratio between the total differential path errors. The PCV term is much smaller than the PCO term in both cases, but it shows the same tendency. Therefore, the larger Genesis error on the Onsala–GGAO baseline is mainly caused by stronger differential phase-centre geometry, not by a larger ordinary baseline projection.

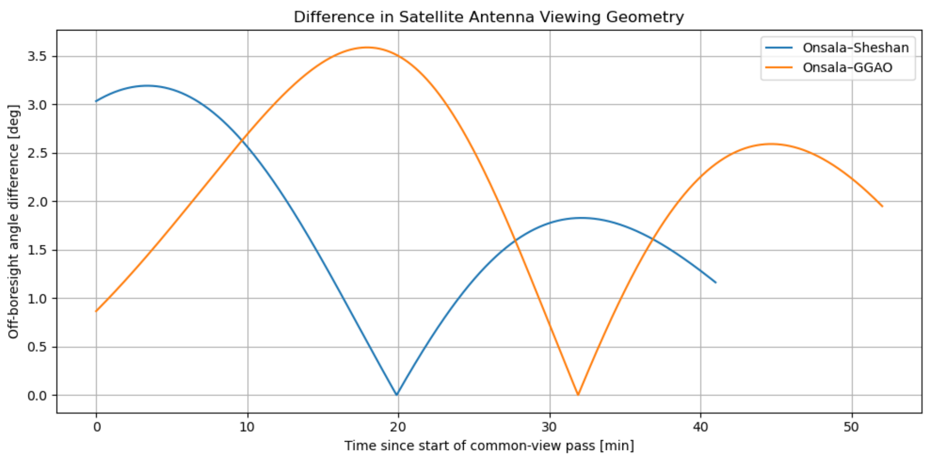

Figure 5.6: Difference in satellite antenna viewing geometry for the longest common-view passes of Onsala–Sheshan and Onsala–GGAO.

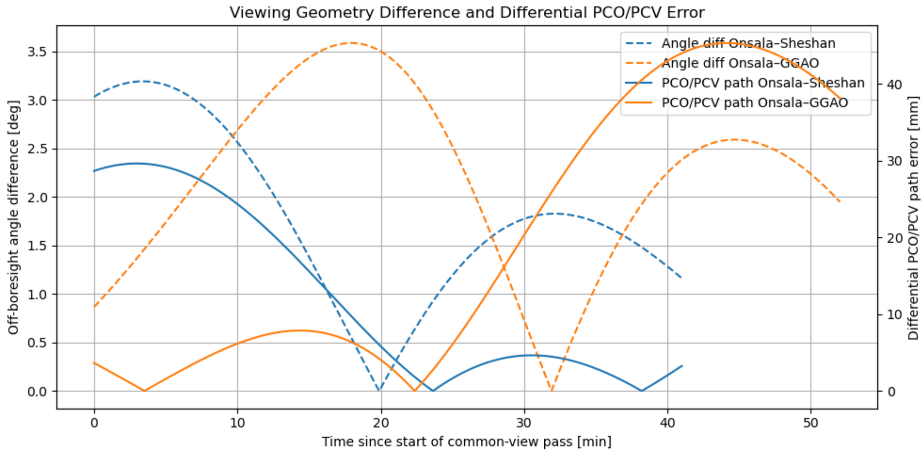

Figure 5.7: Viewing-geometry difference and differential PCO/PCV path error for the Genesis case.

Overall, the Genesis simulation shows that station priority depends on the quantity being evaluated. From the link-budget perspective, GGAO is not the most demanding station. From the phase-centre error perspective, however, Onsala–GGAO is the most sensitive baseline because of its differential off-boresight geometry. This demonstrates why artificial-source VLBI cannot be evaluated using signal strength alone.

5.1.1 Interpretation of the larger Onsala–GGAO phase variation

The Q2 results show that the Onsala–GGAO baseline has the largest pass-relative delay and phase variation in the Genesis simulation. This result may first appear counter-intuitive, because GGAO does not have the largest ordinary baseline geometry with respect to Onsala. Therefore, an additional comparison was made between the Onsala–Sheshan and Onsala–GGAO baselines in order to identify the source of the larger GGAO variation.

The ECEF baseline length is about 7647.80 km for Onsala–Sheshan and 6130.12 km for Onsala–GGAO. Thus, the GGAO baseline is only about 80 percent of the Sheshan baseline length. The ordinary projected baseline length also does not explain the result. Over the full simulated day, the maximum projected baseline is 7551.89 km for Onsala–Sheshan and 6114.48 km for Onsala–GGAO. The mean projected baseline is 3509.91 km for Sheshan and 2760.47 km for GGAO.

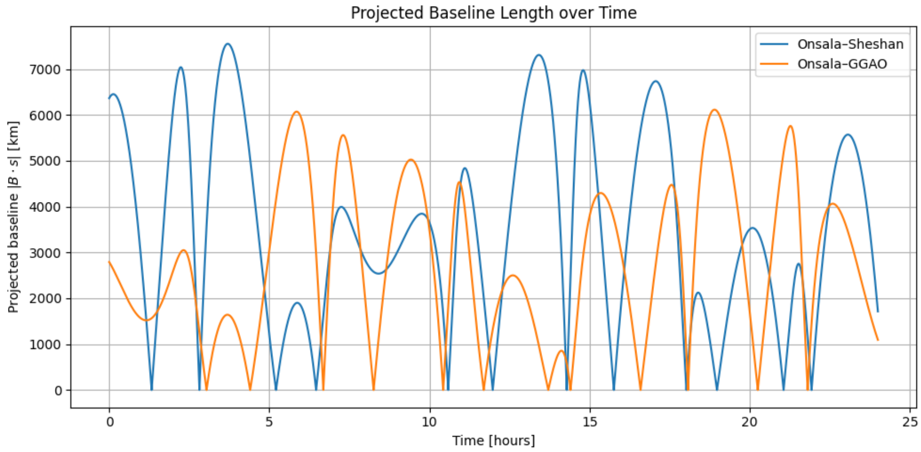

Figure 5.8: Ordinary projected baseline length over the full simulated day for Onsala–Sheshan and Onsala–GGAO.

The same conclusion is obtained when only the common-view windows are considered. During common-view periods, the maximum projected baseline is 5437.91 km for Onsala–Sheshan and 4813.44 km for Onsala–GGAO. The corresponding mean projected baseline values are 3127.82 km and 2130.18 km. Therefore, the larger Q2 delay and phase variation for GGAO cannot be explained by the conventional baseline length or by the ordinary projected baseline length.

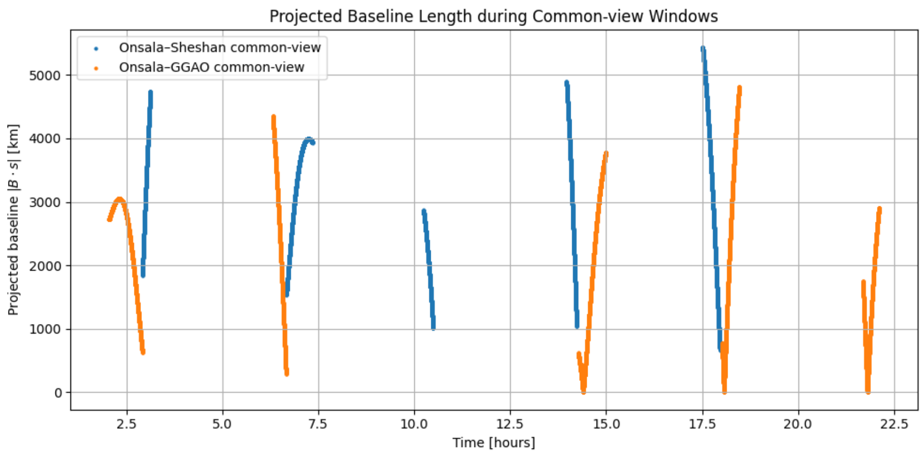

Figure 5.9: Ordinary projected baseline length during common-view windows for Onsala–Sheshan and Onsala–GGAO.

The dominant explanation is instead the differential antenna phase-centre geometry. The two stations in a baseline do not observe the transmitting antenna from exactly the same direction. For a moving satellite, this difference changes during the pass. As shown in Figure 5.5, the maximum off-boresight angle difference is 8.80° for Onsala–Sheshan and 16.02° for Onsala–GGAO. The mean off-boresight angle difference is 2.57° for Sheshan and 4.36° for GGAO. This means that the two stations in the Onsala–GGAO baseline view the satellite antenna from more different directions.

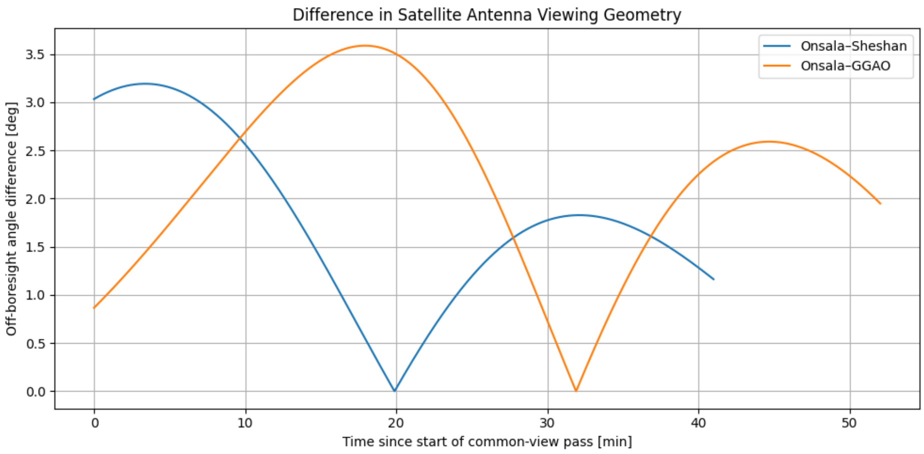

Figure 5.10: Off-boresight angle difference during the longest common-view pass for the two baselines.

With the updated Genesis model, it is also necessary to distinguish between absolute delay error and pass-relative delay variation. The absolute total path maximum is larger for Onsala–Sheshan (1033.79 mm) than for Onsala–GGAO (987.37 mm). However, the pass-relative total path variation is larger for Onsala–GGAO (241.03 mm) than for Onsala–Sheshan (133.93 mm). This is consistent with the Q2 summary, where the total delay variation is 697.82 ps for Sheshan and 819.10 ps for GGAO. The corresponding X-band phase variation is 1953.52° for Sheshan and 2337.30° for GGAO.

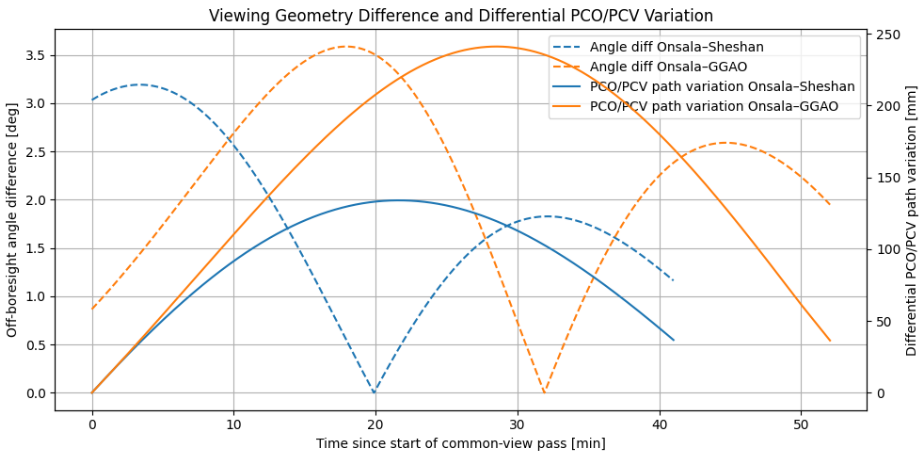

Figure 5.11: Viewing-geometry difference and differential PCO/PCV path variation for Onsala–Sheshan and Onsala–GGAO.

This comparison shows that the larger Q2 delay and phase variation for Onsala–GGAO is not caused by a larger conventional baseline projection. Instead, it is mainly caused by the differential antenna phase-centre geometry. The two stations observe the satellite antenna from more different off-boresight directions, so the projected PCO and PCV contributions vary more strongly during the common-view pass. This explains why GGAO can have favourable link-budget conditions while still producing the largest pass-relative phase-centre variation in the Genesis Q2 analysis.

5.2 Python Simulation Results for the Lunar Station

This section presents the corresponding Python simulation results for the NovaMoon lunar-station scenario. The same reference station and candidate baselines are used as in the Genesis case. The main physical difference is the much larger distance to the transmitter and the slower variation of the source geometry. As a result, the common-view windows are longer, but the required EIRP is much higher than for the Earth-orbiting Genesis source.

The Q1 results show one long common-view pass for each baseline. The longest total common-view duration is obtained for Onsala–Wettzell (39000 s), followed by Onsala–Hartebeesthoek (36360 s), Onsala–GGAO (18840 s), and Onsala–Sheshan (12960 s). The required EIRP is on the order of tens of watts, which is much larger than in the Genesis case. This is expected because the free-space path loss is dominated by the lunar distance.

lunar q1 output table

```
=========== Topic 3 (NovaMoon) Q1 Results ============
Boresight Gain: 29.96 dBi (theta_fwhm = 10.00 deg)
Target spectral flux density: 10.00 Jy
Atmospheric model: P.618 elevation LUT (5.0-90.0 deg, step=2.0 deg)
-------------------------------------------------------

Baseline: Onsala - Wettzell
Number of common-view passes: 1
Total common-view duration: 39000 seconds
Frequency Band  | EIRP_best (W)  | Pt_best (W)  | EIRP_worst (W)  | Pt_worst (W)
-------------------------------------------------------
S-band          | 17.1130        | 0.0173       | 19.4283         | 0.0196
C-band          | 17.3293        | 0.0175       | 20.9776         | 0.0212
X-band-low      | 17.9410        | 0.0181       | 25.3736         | 0.0256
X-band-high     | 18.4012        | 0.0186       | 28.7996         | 0.0291
-------------------------------------------------------

Baseline: Onsala - Sheshan
Number of common-view passes: 1
Total common-view duration: 12960 seconds
Frequency Band  | EIRP_best (W)  | Pt_best (W)  | EIRP_worst (W)  | Pt_worst (W)
-------------------------------------------------------
S-band          | 17.5377        | 0.0177       | 20.9180         | 0.0211
C-band          | 18.1702        | 0.0184       | 27.8394         | 0.0281
X-band-low      | 20.2279        | 0.0204       | 57.8110         | 0.0584
X-band-high     | 21.8163        | 0.0220       | 91.6293         | 0.0925
-------------------------------------------------------

Baseline: Onsala - GGAO
Number of common-view passes: 1
Total common-view duration: 18840 seconds
Frequency Band  | EIRP_best (W)  | Pt_best (W)  | EIRP_worst (W)  | Pt_worst (W)
-------------------------------------------------------
S-band          | 17.2826        | 0.0175       | 20.0159         | 0.0202
C-band          | 17.5888        | 0.0178       | 22.6240         | 0.0229
X-band-low      | 18.3562        | 0.0185       | 28.7414         | 0.0290
X-band-high     | 18.9029        | 0.0191       | 33.4229         | 0.0338
-------------------------------------------------------

Baseline: Onsala - Hartebeesthoek
Number of common-view passes: 1
Total common-view duration: 36360 seconds
Frequency Band  | EIRP_best (W)  | Pt_best (W)  | EIRP_worst (W)  | Pt_worst (W)
-------------------------------------------------------
S-band          | 17.1130        | 0.0173       | 19.5275         | 0.0197
C-band          | 17.3293        | 0.0175       | 21.9281         | 0.0221
X-band-low      | 17.9410        | 0.0181       | 30.3324         | 0.0306
X-band-high     | 18.4012        | 0.0186       | 37.1738         | 0.0375
-------------------------------------------------------
=======================================================
```

Figure 5.12: Python Q1 link-budget output for the NovaMoon lunar-station case.

The frequency dependence is clearly visible. For all baselines, the highest X-band channel requires more EIRP than S-band. The largest worst-case value is found for Onsala–Sheshan, where the highest X-band channel requires 91.63 W EIRP and 0.0925 W transmit power. This behaviour is consistent with larger propagation loss and less favourable elevation or off-axis conditions during part of the common-view interval. In contrast, Onsala–Wettzell has the lowest and most stable power requirement, with a worst-case EIRP of 28.80 W in the highest X-band channel.

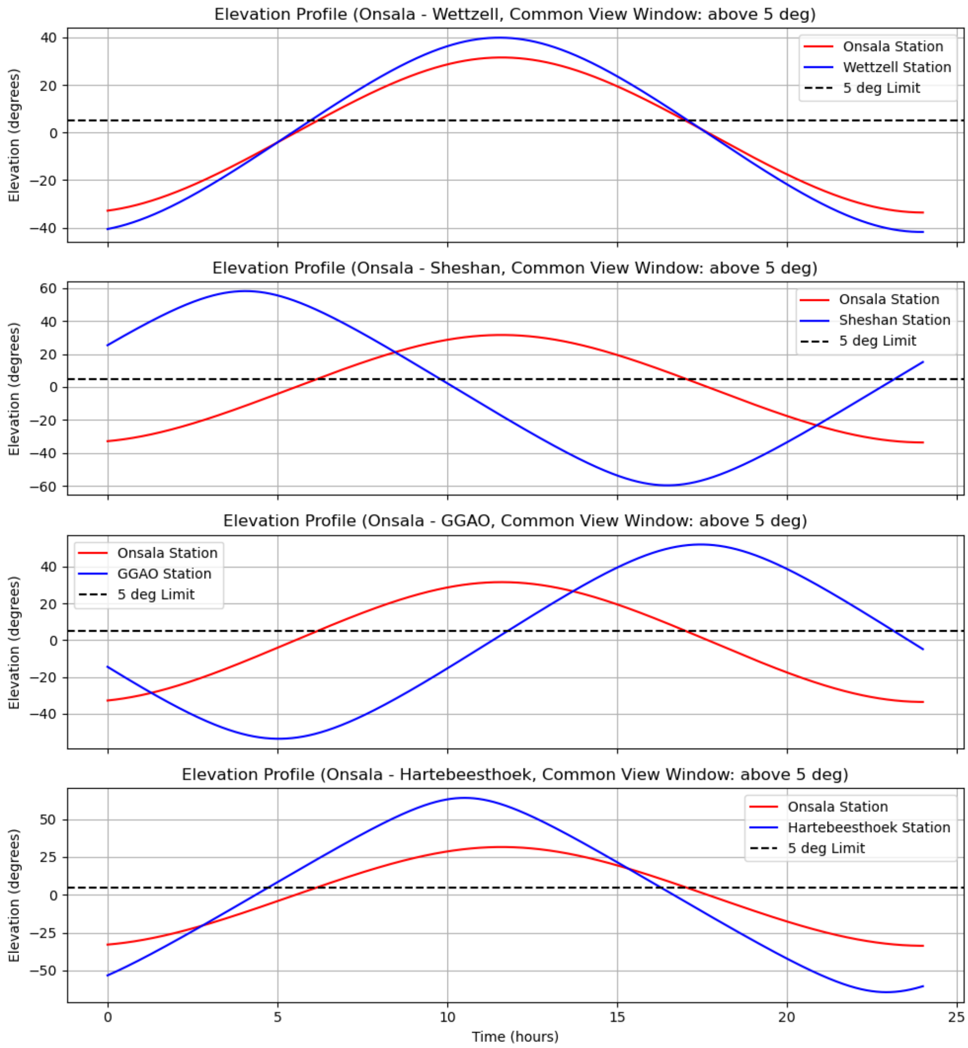

Figure 5.13: Elevation profiles for the NovaMoon common-view windows.

The Q2 results for the lunar-station case are much smaller than for Genesis. The maximum total delay error ranges from 0.36 ps for Onsala–Wettzell to 3.76 ps for Onsala–Hartebeesthoek. The maximum phase error in the highest X-band channel is 1.23° for Onsala–Wettzell, 1.60° for Onsala–Sheshan, 6.02° for Onsala–GGAO, and 12.94° for Onsala–Hartebeesthoek. These values are small compared with the Genesis case because the apparent direction to a lunar-distance transmitter changes slowly during the pass.

lunar q2 output table

```
=========== Topic 3 (NovaMoon) Q2 Results ============

Baseline: Onsala - Wettzell
Max Baseline PCO Delay:   0.36 ps
Max Baseline PCV Delay:   0.00063 ps
Max Total Delay Error:    0.36 ps
Max Phase Error (S-band): 0.41 deg
Max Phase Error (C-band): 0.70 deg
Max Phase Error (X-band-low): 1.05 deg
Max Phase Error (X-band-high): 1.23 deg
-------------------------------------------------------

Baseline: Onsala - Sheshan
Max Baseline PCO Delay:   0.47 ps
Max Baseline PCV Delay:   0.00237 ps
Max Total Delay Error:    0.47 ps
Max Phase Error (S-band): 0.54 deg
Max Phase Error (C-band): 0.91 deg
Max Phase Error (X-band-low): 1.37 deg
Max Phase Error (X-band-high): 1.60 deg
-------------------------------------------------------

Baseline: Onsala - GGAO
Max Baseline PCO Delay:   1.75 ps
Max Baseline PCV Delay:   0.00276 ps
Max Total Delay Error:    1.75 ps
Max Phase Error (S-band): 2.02 deg
Max Phase Error (C-band): 3.42 deg
Max Phase Error (X-band-low): 5.17 deg
Max Phase Error (X-band-high): 6.02 deg
-------------------------------------------------------

Baseline: Onsala - Hartebeesthoek
Max Baseline PCO Delay:   3.76 ps
Max Baseline PCV Delay:   0.00257 ps
Max Total Delay Error:    3.76 ps
Max Phase Error (S-band): 4.34 deg
Max Phase Error (C-band): 7.35 deg
Max Phase Error (X-band-low): 11.11 deg
Max Phase Error (X-band-high): 12.94 deg
-------------------------------------------------------
=======================================================
```

Figure 5.14: Python Q2 phase-centre error output for the NovaMoon lunar-station case.

The baseline delay components show that the PCO contribution is the dominant term, while the PCV contribution is very small. This is true for all baselines. The time variation is smooth because of the slow lunar-source geometry. The phase-error plots also show the expected frequency dependence: higher frequency bands produce larger phase errors for the same delay error.

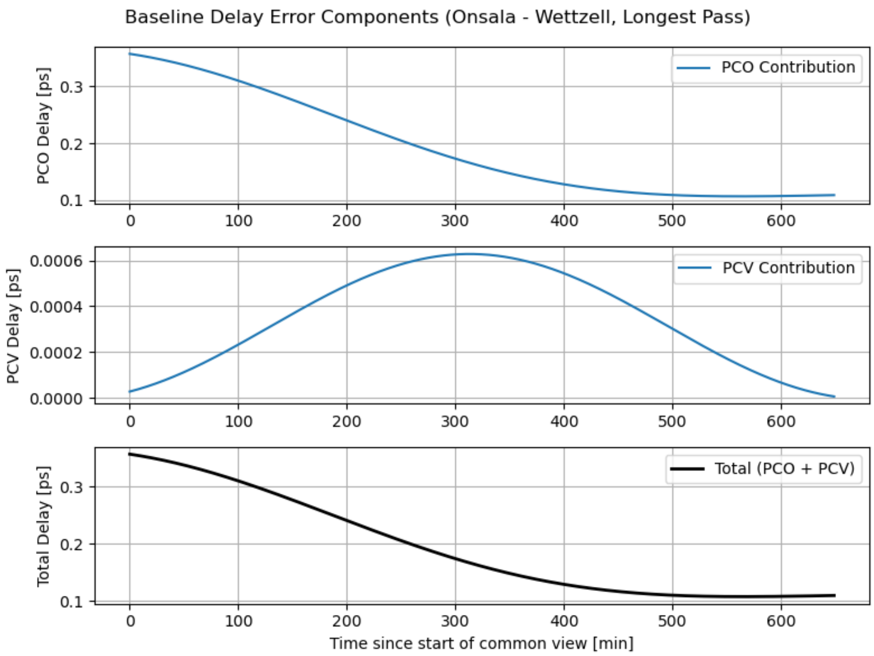

Figure 5.15: Baseline delay error components for Onsala–Wettzell in the NovaMoon case.

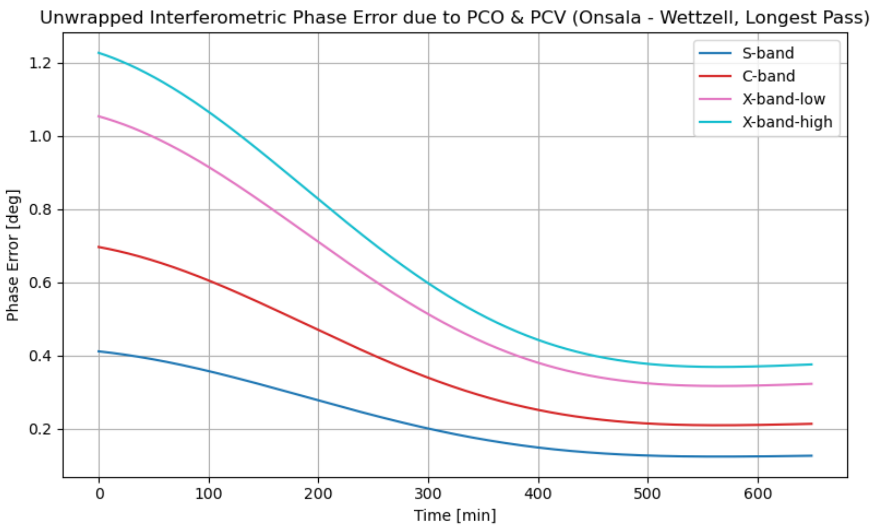

Figure 5.16: Unwrapped interferometric phase error for Onsala–Wettzell in the NovaMoon case.

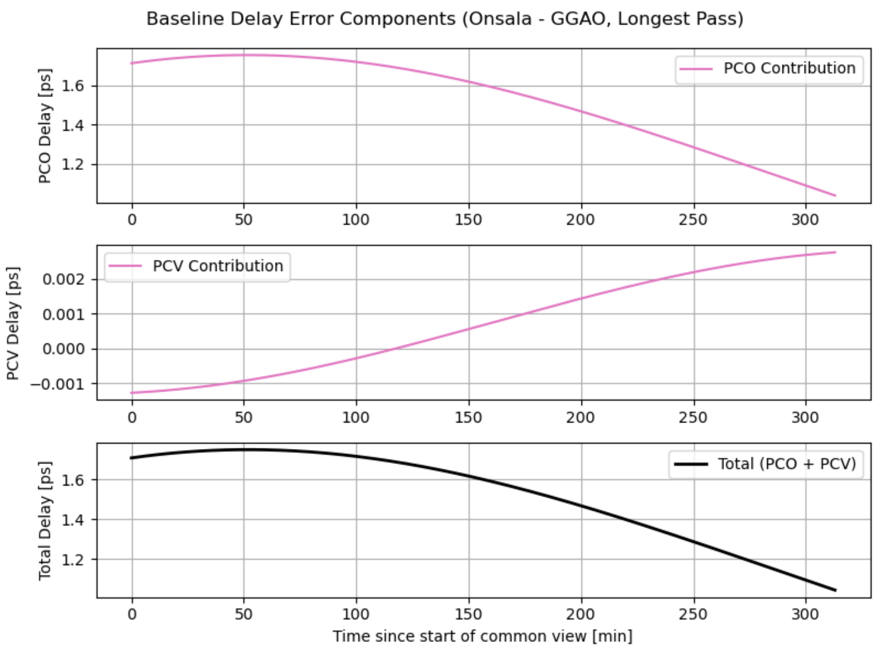

Figure 5.17: Baseline delay error components for Onsala–GGAO in the NovaMoon case.

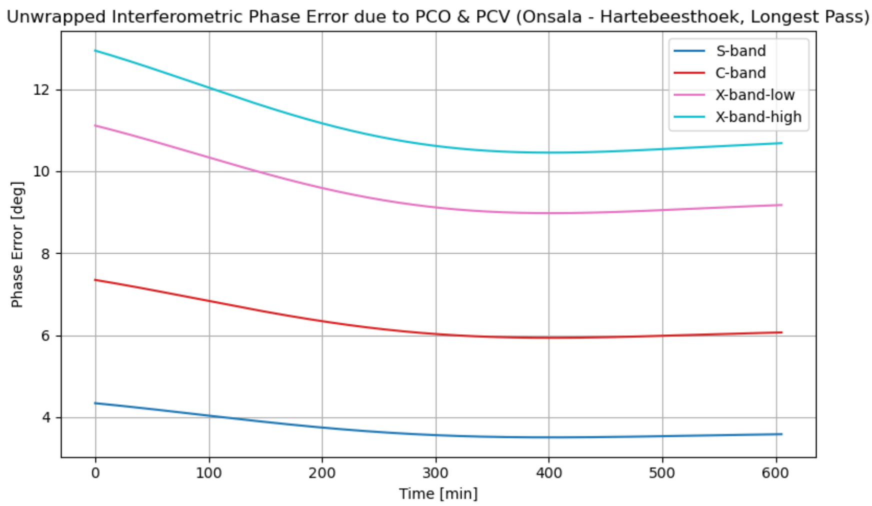

Figure 5.18: Unwrapped interferometric phase error for Onsala–Hartebeesthoek in the NovaMoon case.

The lunar-station results therefore show a different limitation from the Genesis case. For Genesis, the main concern is the rapidly changing viewing geometry and the resulting phase-centre related delay variation. For NovaMoon, the phase-centre errors are small, but the link-budget requirement is much higher because of the lunar distance. The most useful baselines are therefore not identified by a single metric. Onsala–Wettzell is favourable in both common-view duration and link budget, while Onsala–Hartebeesthoek has long visibility but the largest phase-centre error.

Onsala–Sheshan has the highest worst-case power requirement, especially at X-band. These differences motivate the combined comparison with VieSched++ schedules in the following sections.

5.3 VieSched++ Results

This section analyses the seven observation plans at the VieSched++ scheduling level, with emphasis on how different source configurations and station-network scales influence the overall observation-plan structure. The analysis includes scheduling scale, station participation, baseline distribution, source allocation, and multi-station scan structure. These results provide the observation-plan-level foundation for the subsequent accuracy performance analysis in the VieVS simulations.

5.3.1 Overall Comparison of the Observation Plans

This section first compares the seven VieSched++ observation plans from an overall perspective. The seven plans form a progressive experimental design. The first two five-station configurations are used to evaluate the scheduling capability of a basic VGOS subnetwork for a single artificial source. The corresponding sixteen-station configurations are used to assess the improvement in observation opportunities after expanding the station network. The dual-artificial-source configuration is used to investigate the allocation of observation resources when Genesis and NovaMoon are simultaneously present. Finally, the AGN-only and mixed artificial-source and AGN configurations are used to evaluate the scheduling behaviour after introducing conventional celestial radio sources.

Table 5.1 presents the core scheduling statistics of the seven plans. Here, Stations and Sources denote the numbers of participating stations and sources, respectively. Artificial obs. denotes the number of observations of Genesis and/or NovaMoon, while AGN obs. denotes the number of observations of conventional celestial radio sources. This table is to provide an overall scale reference for the subsequent station distribution, baseline distribution, and VieVS simulation results.

Table 5.1: Overall scheduling statistics of the seven VieSched++ observation plans.

Plan	Source configuration	Stations	Sources	Scans	Observations
Genesis-5	Genesis	5	1	31	51
NovaMoon-5	NovaMoon	5	1	47	223
Genesis-16	Genesis	16	1	94	587
NovaMoon-16	NovaMoon	16	1	110	1882
AGN-16	AGN	16	102	1359	18982
Genesis+NovaMoon-16	Genesis + NovaMoon	16	2	275	2579
Genesis+NovaMoon+AGN-16	Genesis + NovaMoon + AGN	16	99	1035	18028

The overall statistics show that the station-network scale has a direct influence on the scheduling output. For the single-source Genesis configuration, increasing the number of stations from five to sixteen increases the number of observations from 51 to 587. For NovaMoon, the number of observations increases from 223 to 1882. The dual-artificial-source configuration further increases the total number of observations, demonstrating that two near-field artificial sources can be jointly scheduled within the same observation plan.

After introducing AGN sources, the total number of observations increases significantly. The AGN-only schedule contains 18982 observations, while the mixed Genesis+NovaMoon+AGN-16 schedule contains 18028 observations, among which the number of artificial-source observations is 349. This indicates that the AGN-containing observation plans are primarily dominated by conventional celestial radio sources, while the mixed observation plan still retains a certain number of observation opportunities for artificial sources.

5.3.2 Station Participation

In addition to the overall scheduling scale, the level of station participation determines the network structure of each observation plan. Since the seven plans differ significantly in their total number of observations, directly comparing the absolute number of observations at each station would cause the large-scale schedules to dominate the comparison. Therefore, this section adopts a normalized comparison based on the station participation share within each observation plan. This quantity is obtained by dividing the $n_{\mathrm{sta\_obs}}$ value of each station by the total $n_{\mathrm{sta\_obs}}$ summed over all stations in the corresponding schedule, thereby representing the relative station-weight distribution within each observation plan.

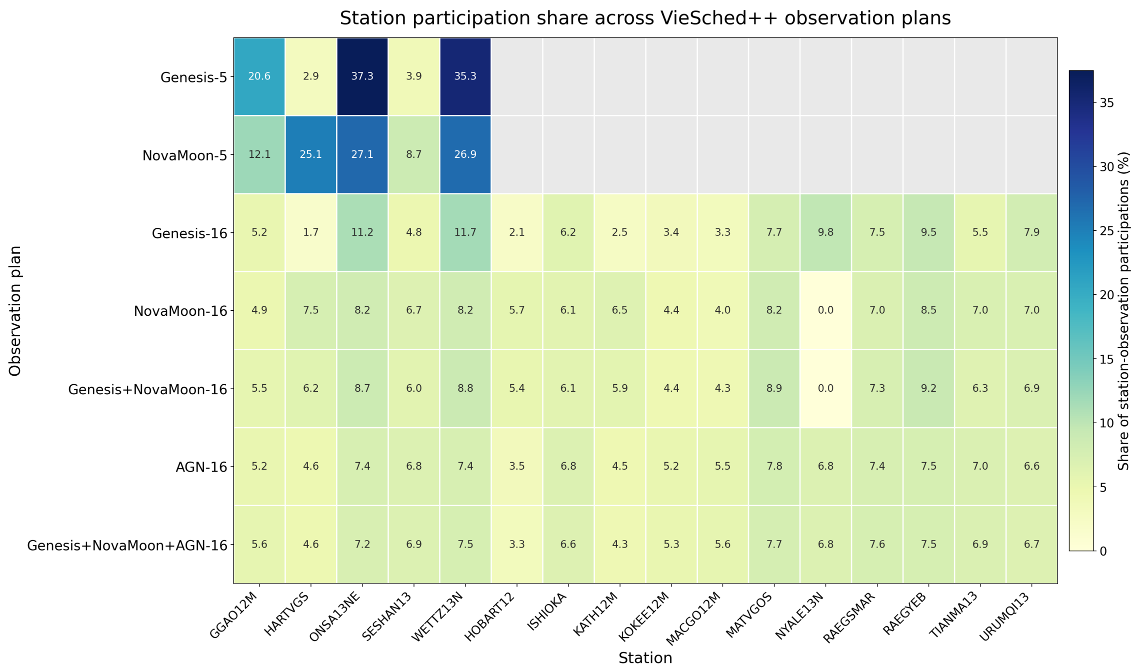

Figure 5.19: Station participation share across the seven observation plans

Figure 5.19 shows that the station participation distribution in the five-station schedules is strongly controlled by the target geometry. For the Genesis five-station schedule, the observations are highly concentrated at ONSA13NE and WETTZ13N, which account for 37.25% and 35.29% of the total station participation, respectively, while HARTVGS and SESHAN13 contribute only 2.94% and 3.92%. This indicates that within the basic five-station network, the rapid motion of Genesis does not provide balanced scheduling opportunities for all stations, but instead causes a small number of geometrically favourable stations to dominate the schedule.

In contrast, the NovaMoon five-station schedule exhibits a more balanced distribution. ONSA13NE, WETTZ13N, and HARTVGS contribute 27.13%, 26.91%, and 25.11%, respectively, indicating that the lunar-surface source provides a more stable, although still not completely uniform, visibility structure within the five-station network.

After expanding the network to sixteen stations, the station participation is no longer dominated by only a few core stations. In the Genesis sixteen-station schedule, WETTZ13N and ONSA13NE still maintain relatively high participation shares of 11.67% and 11.24%, respectively, while NYALE13N, RAEGYEB, URUMQI13, and MATVGOS also reach 9.80%, 9.45%, 7.92%, and 7.67%. This indicates that expanding the station network not only increases the total number of observations, but also significantly redistributes the observation resources across the network.

The NovaMoon sixteen-station schedule exhibits an even smoother participation distribution. Except for NYALE13N, which does not participate, most stations contribute approximately 4%–9%, with RAEGYEB, WETTZ13N, ONSA13NE, and MATVGOS accounting for 8.50%, 8.24%, 8.21%, and 8.21%, respectively. Compared with the five-station NovaMoon schedule, this result demonstrates a more distributed station-contribution structure.

The dual-artificial-source schedule further balances the station participation structure. In the Genesis+NovaMoon schedule, the highest participation share is contributed by RAEGYEB with 9.17%, followed by MATVGOS, WETTZ13N, and ONSA13NE with 8.90%, 8.84%, and 8.70%, respectively. The relatively small differences among these values indicate that the combination of two near-field artificial sources produces a more balanced station-contribution distribution than the single-source schedules. In other words, the dual-source schedule does not merely increase the total number of observations, but also provides a more distributed observation geometry at the network level.

After introducing AGN sources, the station participation distribution becomes even more network-oriented. In the AGN-only schedule, MATVGOS, RAEGYEB, ONSA13NE, WETTZ13N, and RAEGSMAR account for 7.82%, 7.49%, 7.44%, 7.43%, and 7.36%, respectively. In the Genesis+NovaMoon+AGN schedule, most stations contribute approximately 4%–8%, while MATVGOS, RAEGSMAR, WETTZ13N, and RAEGYEB account for 7.69%, 7.61%, 7.51%, and 7.49%, respectively. Compared with the pure artificial-source schedules, the inclusion of AGN sources weakens the control of single-target geometry over the station distribution and allows more stations to participate in a relatively balanced manner. This change is particularly important for the subsequent simulations, because a more balanced station participation structure generally corresponds to more stable network geometry and more reliable parameter-estimation conditions.

Overall, Figure 5.19 demonstrates that the station participation pattern cannot be explained solely by the number of stations. The Genesis five-station schedule exhibits strong station concentration, whereas the NovaMoon five-station schedule is comparatively more balanced. The sixteen-station network significantly expands the available station participation, but different source configurations still produce different participation structures. The dual-artificial-source and AGN-containing schedules further improve the balance of the station distribution. These results indicate that the differences in formal error and repeatability in the subsequent VieVS simulations should be interpreted not only in terms of the total number of observations, but also in terms of the station participation structure.

5.3.3 Baseline Distribution

Although the station participation share reflects the importance of individual stations within an observation plan, the geometric constraints of VLBI observations are ultimately determined by the baseline structure. Therefore, comparing only the number of station observations is still insufficient to describe the network characteristics of the scheduling plans. This section further compares the dominant observation baselines among the seven plans and characterizes the network distribution using the concepts of dominant baselines and active baselines. Here, active baselines denote the number of baselines that obtained at least one observation, while top-five share denotes the fraction of the total observations contributed by the five baselines with the highest observation counts.

Table 5.2 shows that the difference between the five-station and sixteen-station schedules is reflected not only in the total number of observations, but also in the concentration of baseline usage. Genesis-5 forms only 6 active baselines, while the five baselines with the highest observation counts already account for 98.0% of the total observations. In particular, the single baseline ONSA13NE–WETTZ13N contains 23 observations, corresponding to 45.1% of the total 51 observations in the schedule. This indicates that the Genesis scheduling within the basic five-station network is highly dependent on a small number of available baselines, resulting in a relatively concentrated network geometry.

Compared with Genesis-5, NovaMoon-5 is slightly more distributed, although it still exhibits significant baseline concentration. This schedule forms 9 active baselines with a top-five share of 75.8%. ONSA13NE–WETTZ13N remains the dominant baseline with 46 observations, while HARTVGS–WETTZ13N and HARTVGS–ONSA13NE both reach 42 observations. Compared with Genesis-5, the dominant observations in NovaMoon-5 are no longer almost entirely controlled by a single baseline, but instead form a more stable three-station structure among ONSA13NE, WETTZ13N, and HARTVGS.

Table 5.2: Dominant baseline distribution in the seven VieSched++ observation plans.

Plan	Active baselines	Top-five share [%]	Top five baselines
Genesis-5	6	98.0	Oe–Wn (23) Gs–Oe (12) Gs–Wn (9) Oe–S6 (3) Hv–Wn (3)
NovaMoon-5	9	75.8	Oe–Wn (46) Hv–Wn (42) Hv–Oe (42) Gs–Oe (20) Gs–Wn (19)
Genesis-16	75	18.4	Oe–Wn (25) K2–Mg (22) Yj–Wn (21) Oe–Yj (20) Nn–Wn (20)
NovaMoon-16	91	12.0	Yj–Wn (45) Oe–Wn (45) Oe–Yj (45) Mb–Wn (45) Mb–Yj (45)
AGN-16	118	9.6	Sa–Yj (385) Mb–Yj (378) S6–T1 (375) Mb–Sa (345) Mb–Wn (339)
Genesis+NovaMoon-16	93	14.6	Mb–Yj (80) Mb–Wn (79) Yj–Wn (78) Oe–Wn (70) Mb–Oe (69)
Genesis+NovaMoon+AGN-16	118	9.5	Sa–Yj (368) Mb–Wn (344) S6–T1 (342) Mb–Yj (332) Mb–Sa (318)

After expanding the network to sixteen stations, the baseline distribution becomes significantly broader. Genesis-16 increases the number of active baselines to 75, while the top-five share decreases to 18.4%. Although ONSA13NE–WETTZ13N remains the baseline with the largest number of observations, it contains only 25 observations, corresponding to 4.3% of the total 587 observations. This indicates that after network expansion, the observation opportunities of Genesis are no longer concentrated on a few core baselines, but are instead distributed across a much larger network structure.

The distribution of NovaMoon-16 becomes even more balanced. The number of active baselines increases to 91, while the top-five share decreases further to 12.0%. Several dominant baselines contain the same number of observations, namely 45 observations each, indicating that the observation geometry of NovaMoon within the sixteen-station network is not controlled by a single dominant baseline, but instead jointly supported by multiple high-contribution baselines.

The dual-source schedule exhibits baseline characteristics intermediate between the single-source schedules and the AGN-containing schedules. Genesis+NovaMoon-16 forms 93 active baselines with a top-five share of 14.6%, which is higher than NovaMoon-16 but lower than Genesis-16. Its dominant baselines are concentrated among MATVGOS, RAEGYEB, WETTZ13N, and ONSA13NE. For example, MATVGOS–RAEGYEB, MATVGOS–WETTZ13N, and RAEGYEB–WETTZ13N contain 80, 79, and 78 observations, respectively. This indicates that after jointly scheduling the two near-field artificial sources, the network does not simply inherit the structure of a single-source schedule, but instead forms a new combination of high-contribution baselines.

After introducing AGN sources, the baseline distribution reaches the broadest state among all seven schedules. AGN-16 and Genesis+NovaMoon+AGN-16 both form 118 active baselines, while the theoretical maximum number of baselines for a sixteen-station network is 120. This indicates that nearly the entire station network participates in the observations. In the AGN-only schedule, the top five baselines are Sa–Yj, Mb–Yj, S6–T1, Mb–Sa, and Mb–Wn, with a top-five share of 9.6%. In the Genesis+NovaMoon+AGN-16 schedule, several dominant baselines also contain large numbers of observations, such as RAEGSMAR–RAEGYEB with 368 observations and MATVGOS–WETTZ13N with 344 observations, while the total number of observations reaches 18028, resulting in a top-five share of only 9.5%. This demonstrates that the inclusion of AGN sources significantly expands the baseline coverage and shifts the observation plan from a locally concentrated geometry dominated by artificial sources toward a more fully distributed VLBI scheduling structure involving nearly the entire network.

Overall, the baseline results further demonstrate that the quality of an observation plan cannot be evaluated solely by the total number of observations or the number of stations. The primary limitation of the five-station schedules lies in the strong concentration of the baseline structure. The sixteen-station schedules significantly increase the number of active baselines and reduce the dependence on a few dominant baselines. The dual-artificial-source schedule forms new combinations of high-contribution baselines, while the AGN-containing schedules provide the broadest network coverage. These baseline-level differences will directly affect the stability of the station coordinate, EOP, and source coordinate results in the subsequent VieVS simulations.

5.3.4 Source Allocation

The previous results have shown that expanding the station network changes the observation distribution at both the station and baseline levels. However, for observation plans containing multiple targets, it is also necessary to examine how the observation resources are allocated among different source types. Since all observations in the single-source schedules belong to the same target type, the source allocation itself does not provide additional information. Therefore, this section compares the source allocation in the Genesis+NovaMoon, AGN-16, and Genesis+NovaMoon+AGN schedules.

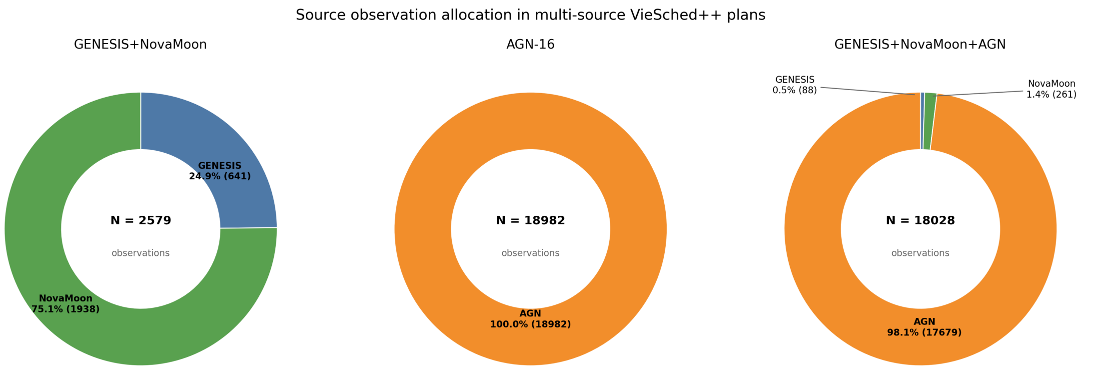

Figure 5.20: Source observation allocation in the VieSched++ observation plans

Figure 5.20 shows that in the dual-artificial-source schedule without AGN, the observation resources are not evenly distributed between Genesis and NovaMoon. This schedule contains a total of 2579 observations, among which NovaMoon obtains 1938 observations, corresponding to 75.1%, while Genesis obtains 641 observations, corresponding to 24.9%. This indicates that when the two near-field artificial sources are simultaneously included in the schedule, VieSched++ does not simply sample the two targets uniformly. Instead, a non-uniform source allocation is formed according to visibility conditions, station availability, and scheduling weights. NovaMoon occupies a larger fraction in this schedule, indicating that under the current configuration it can provide more schedulable multi-station observation opportunities.

In the AGN-16 schedule, all 18982 observations belong to conventional celestial radio sources. This represents the source-allocation structure of the AGN-only sixteen-station schedule, where the observation resources are entirely assigned to reference-source observations.

After introducing AGN sources into the mixed-source schedule, the source allocation structure changes significantly. The Genesis+NovaMoon+AGN schedule contains a total of 18028 observations, among which AGN observations account for 17679 observations, corresponding to 98.1%. In comparison, NovaMoon and Genesis retain only 261 and 88 observations, corresponding to 1.4% and 0.5%, respectively. This result indicates that within the complete mixed-source schedule, conventional celestial radio sources dominate the vast majority of the observation resources. The artificial-source observations do not disappear completely, but their fractions are strongly compressed, indicating that in an AGN-rich scheduling environment the artificial sources behave more as embedded observation targets rather than dominant scheduling objects.

The comparison among these schedules reveals an important pattern: the competition between artificial sources and the competition between artificial sources and AGN are fundamentally different in nature. In the Genesis+NovaMoon schedule, the observation resources are mainly redistributed between the two near-field targets. Although NovaMoon dominates the schedule, Genesis still retains approximately one quarter of the observation share. In the AGN-16 schedule, the observation resources are fully assigned to conventional celestial radio sources. After AGN are introduced into the mixed-source schedule, the competing targets change from artificial sources alone to a large number of conventional celestial radio sources, causing the scheduling resources to rapidly shift toward AGN observations. In other words, the introduction of AGN does not merely increase the number of sources, but instead changes the entire source-allocation structure of the observation plan.

Therefore, Figure 5.20 supports a key assumption used in the subsequent simulation analysis: although the AGN-containing mixed schedule retains artificial-source observations, its primary role has already shifted from an artificial-source observation plan toward a mixed reference-frame observation plan. The advantage of this schedule is not to maximize the number of Genesis or NovaMoon observations, but rather to simultaneously provide artificial-source observations and conventional celestial-source constraints, thereby offering a more complete observation structure for the subsequent EOP, source coordinate, and station coordinate simulations.

5.3.5 Scan Multiplicity and Multi-Station Participation

In addition to the station and baseline distributions, the number of participating stations within each scan is also an important indicator of observation-plan quality. In VLBI scheduling, a two-station scan can produce only a single baseline, whereas a multi-station scan can simultaneously contribute multiple baselines and provide stronger network geometric constraints. Therefore, this section uses scan multiplicity to compare the relative distributions of two-station, three-station, four-station, five-station, and six-or-more-station scans among the seven observation plans.

Figure 5.21 shows that the Genesis and NovaMoon schedules within the five-station network exhibit significantly different scan structures. Genesis-5 contains a total of

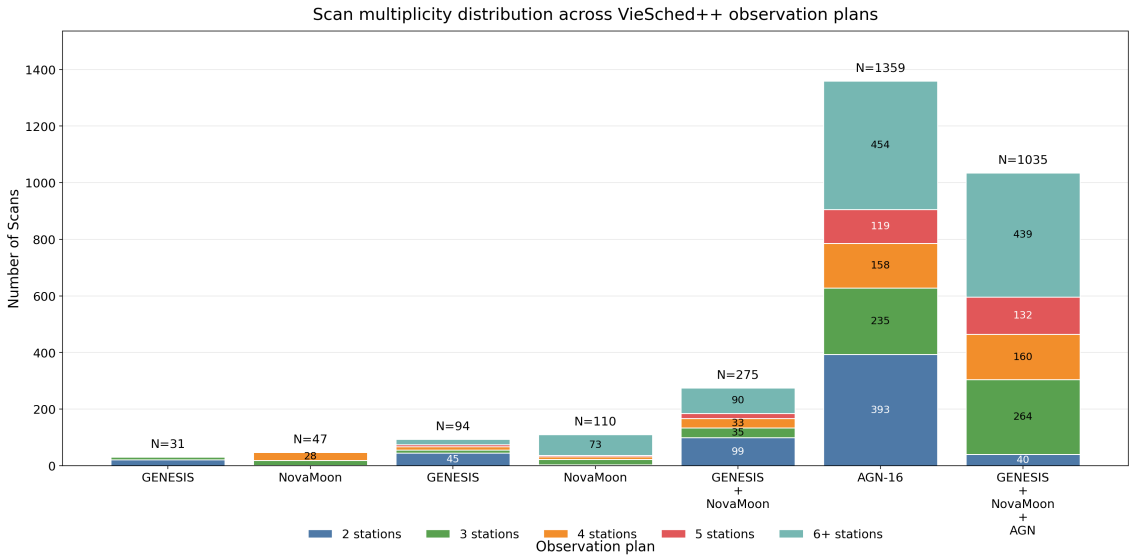

Figure 5.21: Scan multiplicity distribution across the seven VieSched++ observation plans

31 scans, among which 21 are two-station scans, corresponding to 67.7%, while the remaining 10 are three-station scans, corresponding to 32.3%. This indicates that within the basic five-station network, the Genesis schedule is primarily composed of low-multiplicity scans, resulting in relatively weak network geometric constraints.

In contrast, NovaMoon-5 contains a total of 47 scans, among which 28 are four-station scans, corresponding to 59.6%, while 18 are three-station scans, corresponding to 38.3%. Only a single two-station scan is present. This indicates that although the total observation scale of NovaMoon-5 remains limited, the degree of multi-station participation within individual scans is significantly higher than in Genesis-5.

After expanding the network to sixteen stations, the scan multiplicity of both single-source schedules changes substantially. In Genesis-16, two-station scans still account for the largest fraction, with 45 scans corresponding to 47.9%, while scans involving six or more stations account for 19 scans, corresponding to 20.2%. This indicates that although the expanded network provides more multi-station observation opportunities for Genesis, its rapid-motion characteristics still cause many scans to remain low-station-count structures.

NovaMoon-16 exhibits much stronger multi-station characteristics. Among the 110 scans, 73 belong to the six-or-more-station category, corresponding to 66.4%, while only 3 scans are two-station scans, corresponding to 2.7%. This further demonstrates that NovaMoon can more easily form simultaneous multi-station observations within the sixteen-station network.

The dual-artificial-source schedule exhibits a structure intermediate between the Genesis and NovaMoon single-source schedules. Genesis+NovaMoon-16 contains a total of 275 scans, among which 99 are two-station scans, corresponding to 36.0%, while 90 scans involve six or more stations, corresponding to 32.7%. This result indicates that the dual-source schedule is neither completely dominated by the high-multiplicity characteristics of NovaMoon nor simply a repetition of the low-multiplicity Genesis structure. Instead, it forms a mixed distribution containing both low-station-count and high-station-count scans. This is consistent with the previous source-allocation results, where the two artificial sources jointly influence the scheduling structure within the same observation plan.

After introducing AGN sources, the scan multiplicity distribution shows a substantially larger scan scale. The AGN-16 schedule contains a total of 1359 scans, among which 393 are two-station scans, corresponding to 28.9%, while 454 scans involve six or more stations, corresponding to 33.4%. The numbers of three-station, four-station, and five-station scans are 235, 158, and 119, respectively. Genesis+NovaMoon+AGN-16 contains a total of 1035 scans, among which 439 involve six or more stations, corresponding to 42.4%. The numbers of three-station, four-station, and five-station scans are 264, 160, and 132, respectively, while only 40 scans are two-station scans, corresponding to 3.9%. This indicates that the inclusion of AGN sources not only increases the total number of scans, but also changes the relative proportion of low-station-count and high-station-count scans, making the overall schedule more similar to the multi-station observation structure of conventional geodetic VLBI.

Overall, the variation in scan multiplicity reveals the differences in network geometry among the observation plans. The Genesis single-source schedules tend to produce two-station or low-station-count scans, especially within the five-station network. Although the NovaMoon single-source schedules still face other solution limitations, they are more likely to form multi-station scans at the scheduling level. The dual-artificial-source schedule produces a mixed structure containing both low-station-count and high-station-count scans, while the AGN-containing schedules significantly increase the scan scale and strengthen multi-station participation.

These results indicate that the quality of an observation plan cannot be evaluated solely by the total numbers of scans or observations. It is also necessary to consider the actual number of participating stations within each scan, because this directly affects the number of available baselines and the geometric stability of the subsequent simulations.

5.3.6 Summary of Scheduling Patterns

Overall, the seven VieSched++ observation plans demonstrate different scheduling structures at the levels of network scale, source configuration, and multi-station participation. The five-station schedules are primarily intended to characterize the feasibility of artificial-source observations within a basic network configuration, while the sixteen-station schedules significantly expand the available station and baseline space.

Genesis and NovaMoon exhibit different characteristics in terms of station participation, dominant baselines, and scan multiplicity, indicating that near-Earth satellite sources and lunar-surface sources cannot simply be treated as the same category of artificial source. The dual-artificial-source schedule demonstrates that two near-field targets can be jointly scheduled within the same observation plan, but the resulting observation-resource allocation and network structure are not simple combinations of the two single-source schedules.

After introducing AGN sources, the scheduling structure shifts toward observation modes dominated by conventional celestial radio sources. The AGN-only schedule shows the reference-source scheduling structure within the sixteen-station network, while the mixed Genesis+NovaMoon+AGN schedule still retains limited but clearly identifiable observation opportunities for artificial sources. These scheduling differences form the observational basis for the subsequent differences in formal error and repeatability observed in the VieVS simulations.

5.4 VievS Simulation Results

This section evaluates the parameter-estimation performance of the observation plans based on the simulation outputs of VieVS. Unlike the VieSched++ analysis, which focuses on scheduling structure, this section compares station-coordinate formal error and repeatability.

The VieVS analysis is limited to six plans: Genesis-5, NovaMoon-5, Genesis-16, NovaMoon-16, Genesis+NovaMoon-16, and Genesis+NovaMoon+AGN-16. The AGN-16 schedule is not processed in VieVS because it is used here mainly as a conventional reference for the scheduling comparison, while the VieVS analysis focuses on artificial-source-only and artificial-source-assisted plans.

The simulation error sources applied in VieVS include clock errors, tropospheric errors, and white noise. The subsequent estimation results therefore reflect the station-coordinate solution performance after the introduction of these error contributions.

5.4.1 Overall Comparison of VieVS Simulation Results

In this section, station-coordinate formal error and repeatability are reported as three-dimensional station-coordinate quantities derived from the VieVS output, where the X, Y, and Z coordinate components are combined into one 3D coordinate value for each station. Table 5.3 summarizes the core estimation results obtained after the six observation plans were processed. The retained metrics focus on the station coordinate formal error and repeatability.

The results in the table show that the different observation plans exhibit significant differences in station coordinate estimation performance. Although the five-station schedules can complete the VieVS simulation workflow, their station coordinate

Table 5.3: Overall VieVS station-coordinate simulation results for the six observation plans.

Plan	Station formal error [mm]	Station repeatability [mm]
Genesis-5	5.43×10^8	1.08×10^8
Genesis-16	367.6	319.8
NovaMoon-5	5.02×10^7	6.07×10^7
NovaMoon-16	1.10×10^6	3.94×10^6
Genesis+NovaMoon-16	82.8	151.9
Genesis+NovaMoon+AGN-16	33.2	31.8

results remain highly unstable. The formal errors of Genesis-5 and NovaMoon-5 reach 5.43×10^8 mm and 5.02×10^7 mm, respectively, indicating that the basic five-station network is insufficient to provide stable station-coordinate constraints.

After expanding the network to sixteen stations, the formal error and repeatability of Genesis-16 decrease to 367.6 mm and 319.8 mm, respectively, demonstrating that network expansion significantly improves the near-Earth satellite configuration.

However, the results of NovaMoon-16 remain relatively weak, with a formal error of 1.10×10^6 mm and a repeatability of 3.94×10^6 mm. This indicates that a larger observation scale does not necessarily lead to more stable estimation results, and that the geometric characteristics of the lunar-surface source still limit the estimability of the station coordinates.

In contrast, the results of Genesis+NovaMoon-16 improve significantly, with the formal error and repeatability decreasing to 82.8 mm and 151.9 mm, respectively. This indicates that the dual-artificial-source configuration provides more stable network constraints than the standalone NovaMoon configuration.

Genesis+NovaMoon+AGN-16 produces the most stable station coordinate results among all six schedules, with a formal error of 33.2 mm and a repeatability of 31.8 mm. The advantage of this schedule is reflected not only in the lowest numerical values, but also in the completeness of its solution structure.

5.4.2 Station-Level Repeatability Distribution

To further determine whether the station coordinate estimation performance is dominated by only a small number of stations, this section presents the repeatability distribution at the station level. Compared with average values, station-by-station repeatability more directly reflects the internal network stability of each observation plan and reveals whether strong imbalance exists among different stations. Since the numerical ranges vary substantially among the schedules, Figure 5.22 uses a logarithmic colour scale to display the station coordinate repeatability.

Figure 5.22 shows that the five-station schedules exhibit clear instability in the

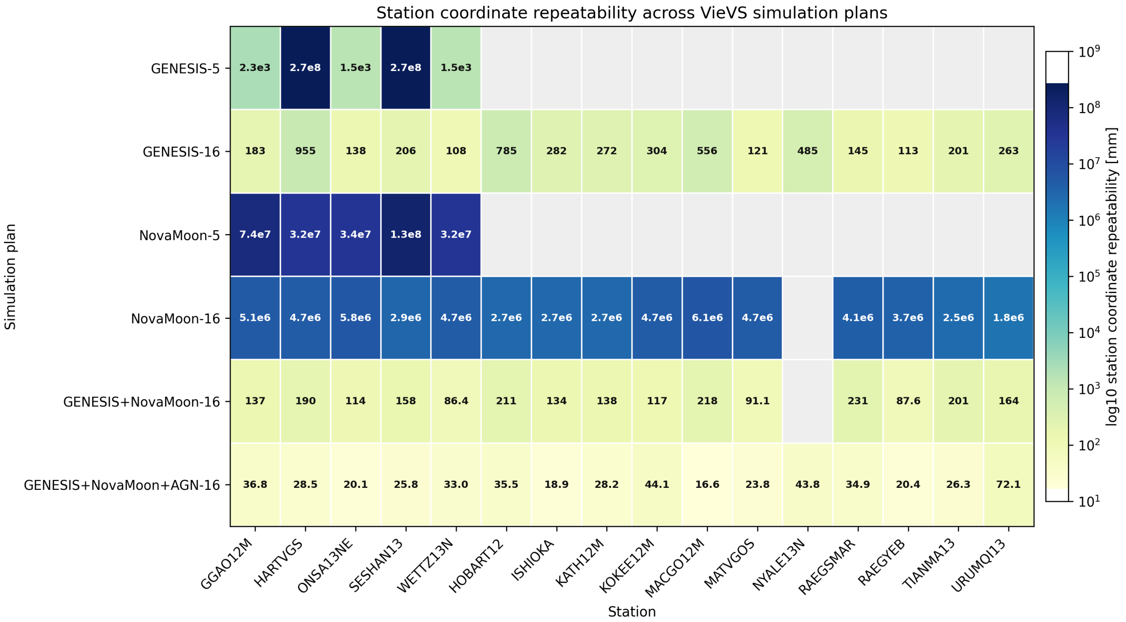

Figure 5.22: Station-level 3D coordinate repeatability obtained from VieVS simulation results

station-level repeatability distribution. In Genesis-5, the repeatability of HARTVGS and SESHAN13 reaches approximately 2.7×10^8 mm, while GGAO12M, ONSA13NE, and WETTZ13N remain at approximately the 10^3 mm level. This indicates that the average result of Genesis-5 does not uniformly represent the performance of all stations, but is instead strongly affected by a small number of extremely unstable stations.

In NovaMoon-5, all five stations remain within the range of approximately 10^7–10^8 mm, indicating that the instability of this schedule is more global in nature rather than being concentrated at a few individual stations.

After expanding the network to sixteen stations, the performances of Genesis and NovaMoon diverge significantly. Most stations in Genesis-16 decrease to the several-hundred-millimetre level, with WETTZ13N and RAEGYEB reaching approximately 108 mm and 113 mm, respectively, indicating relatively stable station coordinate repeatability.

In contrast, although NovaMoon-16 contains more stations, the repeatability of most stations still remains at approximately the 10^6 mm level. This indicates that the weak stability of the lunar-surface-source schedule is not caused by a single anomalous station, but instead reflects a generally weak station-level estimation structure across the entire network.

The dual-artificial-source schedule significantly improves the station-level distribution. In Genesis+NovaMoon-16, most stations decrease to approximately the 10^2 mm level. The lowest repeatability values are obtained for WETTZ13N and RAE-

GYEB, at approximately 86 mm and 88 mm, respectively, while the highest value, corresponding to RAEGSMAR, is still only approximately 231 mm. Compared with NovaMoon-16, this result indicates that the inclusion of Genesis significantly strengthens the network geometric constraints, preventing the lunar-source-related schedule from remaining at the million-millimetre instability level.

Genesis+NovaMoon+AGN-16 produces the most balanced station-level results. This distribution indicates that the AGN-mixed schedule not only reduces the average repeatability, but also makes the station-level results more uniform. This property is more important than the average value alone, because it demonstrates that the stability improvement originates from the enhancement of the overall network structure rather than from only a few well-performing stations reducing the average result.

Overall, the station-level heatmap further demonstrates that the differences in the VieVS simulation results cannot be explained solely by the number of observations. Genesis-16, Genesis+NovaMoon-16, and Genesis+NovaMoon+AGN-16 progressively exhibit more stable and more balanced station coordinate results, whereas the NovaMoon-only schedules remain weak in station-level repeatability even after network expansion.

5.4.3 Summary of VieVS Simulation Results

The VieVS simulation results demonstrate that the geometric structure of the observation plans has a decisive influence on the stability of station coordinate estimation. Although the five-station schedules are able to complete the estimation process, their repeatability is highly sensitive to individual stations, especially in Genesis-5 and NovaMoon-5, where clear instability is observed.

After expanding the network to sixteen stations, the station coordinate repeatability of the Genesis-only schedule improves significantly. In contrast, the NovaMoon-only schedule still maintains relatively large error levels even after increasing the number of stations, indicating that lunar-surface-source observations are intrinsically more sensitive to network geometry and estimation conditions.

Compared with the single-source schedules, both Genesis+NovaMoon-16 and Genesis+NovaMoon+AGN-16 exhibit more stable station distributions. Among them, the mixed schedule containing AGN sources produces the lowest and most uniform station coordinate repeatability.

Overall, the VieVS results further demonstrate that simply increasing the number of observations is insufficient to guarantee stable estimation performance. Instead, the combined effects of source-type configuration and station-network geometry are the key factors influencing the simulation performance.

6

Conclusion

6.1 Feasibility and Stability of Artificial-Source VLBI

This study evaluates artificial VLBI transmitter sources from three perspectives: physical simulation, observation scheduling, and estimation stability. These three analysis stages are not independent of each other, but instead form a continuous evaluation framework ranging from "whether the signal is physically observable," to "whether the observations can be scheduled," and finally to "whether the parameter estimation is stable." The Python simulations define the physical boundaries of artificial-source observations, VieSched++ reveals how these observation opportunities are organised under practical scheduling constraints, and the VieVS simulations further examine the stability of different observation plans in station-coordinate estimation.

Overall, Genesis and NovaMoon represent two fundamentally different types of artificial VLBI transmitter sources. As a near-Earth moving source, Genesis requires a relatively low link budget and is therefore easier to observe in terms of signal strength. However, its rapidly changing observation geometry makes phase-centre-related errors and low-multiplicity scans more prominent. This indicates that the main limitation of near-Earth artificial sources is not signal power itself, but rather the influence of rapid apparent motion on observation geometry and error propagation.

In contrast, NovaMoon provides more stable common-view geometry and more easily forms multi-station scans within the observation schedules. However, the lunar distance introduces significantly higher link-budget requirements. At the same time, the VieVS results show that the NovaMoon-only schedules still struggle to achieve stable station-coordinate estimation even after network expansion. This indicates that the advantages of distant artificial sources cannot be directly translated into improved estimation performance, since their geometric constraint capability is still limited by the combined effects of source location, station-network distribution, and orbital modelling.

The scheduling results obtained from VieSched++ further demonstrate that station-network scale and source configuration significantly influence the structure of artificial-source observations. After expanding the network from five to sixteen stations, the available station and baseline space increases substantially, and the observation plans evolve from structures dominated by a few core stations and dominant baselines into more distributed network configurations. However, increasing the number of stations alone does not guarantee stable estimation performance. Genesis exhibits clear improvement within the sixteen-station network, whereas the NovaMoon-only schedules still maintain relatively weak station-coordinate repeatability. This indicates that observation quantity and multi-station participation are necessary conditions, but not sufficient conditions. The actual estimation quality is determined by the combined relationship among source geometry, network configuration, and observation constraints.

The mixed-source schedules provide results that are closer to practical applications. The Genesis+NovaMoon schedule demonstrates that the two artificial-source types can be jointly scheduled within the same observation plan, while also providing a more stable estimation structure than the standalone NovaMoon schedules. After further introducing AGN sources, although most observation resources shift toward the conventional celestial sources, the overall station-coordinate repeatability becomes more uniform and stable. This indicates that AGN sources are not merely background targets competing with artificial sources for observation time, but instead provide essential reference-frame constraints within mixed observation schedules. For future artificial-source VLBI applications, artificial-source observations should therefore not be designed as isolated single-target experiments, but should instead be jointly optimised together with conventional celestial sources and the overall station-network structure.

Therefore, the overall conclusion of this study is that the feasibility of artificial VLBI transmitter sources cannot be determined by a single metric. The link budget determines whether the signal can be physically received, the common-view windows and scheduling results determine whether the observations can be practically realised, and the formal error and repeatability determine whether the observation plan provides stable estimation capability. Only when all three levels are simultaneously satisfied can artificial sources become practically valuable supplementary observation targets for future geodetic VLBI.

6.2 Implications for Observation Planning

Observation planning for artificial VLBI transmitter sources must simultaneously consider signal receivability, scheduling feasibility, and parameter-estimation stability. Optimising only for visibility, observation quantity, or the fraction of multi-station scans is insufficient. The results of this study show that a larger observation scale does not necessarily correspond to more stable station-coordinate estimation. For near-field artificial sources, the effectiveness of an observation plan is jointly determined by source-motion characteristics, station-network geometry, baseline distribution, and reference-source constraints. Therefore, future artificial-source VLBI scheduling should move beyond simply increasing observation opportunities and instead focus on optimising the observation structure and estimation constraints.

As two different types of artificial sources, Genesis and NovaMoon each possess distinct characteristics. The primary advantage of Genesis lies in its relatively low link-budget requirements, but its rapid apparent motion requires scheduling strategies that can adapt to short-duration and rapidly changing common-view geometry. NovaMoon provides longer common-view durations and more easily forms multi-station scans, but its link-budget requirements and station-coordinate estimation stability remain more challenging. This indicates that observation plans for artificial sources should be designed according to the characteristics of the specific source type, rather than relying on a single unified scheduling strategy for all artificial sources.

Mixed-source observations represent a more practical direction for incorporating artificial VLBI transmitter sources into real geodetic observation schedules. Single-artificial-source schedules are useful for isolating and analysing the observation characteristics of a specific target, but their network-constraint capability remains limited. In contrast, the combined scheduling of artificial sources and AGN sources can preserve artificial-source observation opportunities while simultaneously introducing the reference-frame constraints provided by conventional celestial sources, thereby improving the overall estimation stability. Therefore, artificial sources are more suitable as enhancement targets within conventional VLBI observation schedules rather than as independent observation targets intended to completely replace AGN sources.

6.3 Limitations and Future Work

The analyses presented in this study are still subject to several modelling and software limitations. First, both the Genesis and NovaMoon physical models rely on simplified assumptions. Genesis is represented as an idealised near-Earth moving source, while NovaMoon is represented as a fixed artificial transmitter on the lunar surface. These models support controlled comparative analysis, but they do not yet fully include orbital errors, attitude errors, transmitter hardware characteristics, or timing-synchronisation errors that may appear in real missions. Therefore, the results obtained in this study should be regarded as an initial evaluation of the observation potential of artificial-source VLBI rather than as a final prediction of actual mission performance.

Second, the current software workflow still contains input and modelling limitations for non-standard artificial sources. VieSched++ mainly handles moving targets through TLE files, which means that NovaMoon can only be represented approximately during the scheduling stage and cannot fully reproduce the behaviour of a true fixed lunar-surface station. VieVS simulations can be used to evaluate the station coordinate formal error and repeatability of different observation plans, but the processing strategy still relies on the existing VLBI estimation framework, whose support for artificial-source geometry and near-field observation models remains incomplete. These limitations imply that a certain level of modelling inconsistency still exists between the scheduling results and the estimation results.

Future work should proceed in three main directions. First, more accurate artificial-source ephemeris and attitude models should be introduced in order to reduce the biases caused by TLE approximations and simplified geometric models. Second, more realistic transmitter and antenna models should be developed, including frequency configuration, transmission power, antenna radiation patterns, phase-centre offsets, and phase-centre variations. Third, the joint scheduling strategy for artificial sources and AGN sources should be further optimised so that the scheduling objectives consider not only observation quantity, but also link conditions, station-network geometry, and parameter-estimation stability simultaneously. Through these improvements, the practical value of artificial VLBI transmitter sources in future geodetic observation schedules can be evaluated more reliably.

Bibliography

[1] Delva, P. et al. (2023) GENESIS: co-location of geodetic techniques in space. *Earth, Planets and Space*, 75:5.

[2] Schuh, H. and Böhm, J. (2013) Very Long Baseline Interferometry for geodesy and astrometry. In: *Sciences of Geodesy II*. Springer.

[3] Nothnagel, A. et al. (2023) Elements of geodetic and astrometric Very Long Baseline Interferometry. *Journal of Geodesy*, 97:79.

[4] Petit, G. and Luzum, B. (eds.) (2010) IERS Conventions (2010). *IERS Technical Note*, 36.

[5] Krásná, H. et al. (2023) VLBI celestial and terrestrial reference frames VIE2022b. *Astronomy & Astrophysics*, 679:A53.

[6] Schartner, M. and Böhm, J. (2019) VieSched++: A new VLBI scheduling software for geodesy and astrometry. *Publications of the Astronomical Society of the Pacific*, 131:084501.

[7] Petrachenko, B. et al. (2009) Design aspects of the VLBI2010 system. *NASA Technical Memorandum*, NASA/TM-2009-214180.

[8] International Telecommunication Union (2019) Calculation of free-space attenuation. *Recommendation ITU-R P.525-4*.

[9] International Telecommunication Union (2017) Propagation data and prediction methods required for the design of Earth-space telecommunication systems. *Recommendation ITU-R P.618-13*.

[10] International Telecommunication Union (2022) Attenuation by atmospheric gases and related effects. *Recommendation ITU-R P.676-13*.

[11] International Telecommunication Union (2023) Attenuation due to clouds and fog. *Recommendation ITU-R P.840-9*.

[12] Swinburne University of Technology (2026) Jansky. *COSMOS – The SAO Encyclopedia of Astronomy.*

[13] International GNSS Service (2026) Antenna Working Group. *International GNSS Service.*

[14] European Space Agency (2026) Antenna Phase Centre. *Navipedia.*

[15] Zhou, R. et al. (2022) Consistency analysis of the GNSS antenna phase center correction models. *Remote Sensing*, 14(3):540.

A

Supporting Material

A.1 Station Parameters

This appendix contain the ground station coordinates, SEFD values and antenna parameters used in the simulations and schedules.

Table A.1: Station parameters used in the VieSched++ observation plans.

Station	Lat. [deg]	Lon. [deg]	Diameter [m]	SEFD X [Jy]	SEFD S [Jy]
GGAO12M	39.02	76.83	12.0	2800	2100
HARTVGS	-25.89	332.31	13.2	2600	3100
HOBART12	-42.80	212.56	12.0	4300	5300
ISHIOKA	36.21	219.78	13.2	2300	2200
KATH12M	-14.38	227.85	12.0	4800	4800
KOKEE12M	22.13	159.66	12.0	3000	2300
MACGO12M	30.40	104.01	12.0	3000	1700
MATVGOS	40.65	343.30	13.2	1600	1700
NYALE13N	78.94	348.15	13.2	2800	1900
ONSA13NE	57.39	348.08	13.2	2000	2900
RAEGSMAR	36.99	25.13	13.2	1600	1600
RAEGYEB	40.52	3.09	13.2	2800	1900
SESHAN13	31.10	238.80	13.0	3000	3000
TIANMA13	31.09	238.86	13.2	3000	3000
URUMQI13	43.47	-87.17	13.0	3000	3000
WETTZ13N	49.15	347.12	13.2	2500	2500

A.2 Artificial-Source Inputs

The artificial-source inputs used in the VieSched++ observation plans are listed below. The same TLE definitions were used for the single-source, dual-source, and AGN-assisted schedules where applicable.

Table A.2: Artificial-source TLE input files used in the VieSched++ schedules.

Input case	File name
GENESIS-only	`GENESIS_TARGET.tle`
NovaMoon-only	`NOVAMOON_TARGET.tle`
GENESIS+NovaMoon	`GENESIS_NOVAMOON_TARGETS.tle`
GENESIS+NovaMoon+AGN	`GENESIS_NOVAMOON_AGN.tle`

GENESIS TLE

```
GENESIS_TARGET
1 99001U 26001A   26001.00000000  .00000000  00000-0  00000-0 0  9997
2 99001  95.5000   0.0000 0000000   0.0000 180.0000  6.30950882    00
```

NovaMoon TLE

```
NOVAMOON_TARGET
1 99003U 26003A   26001.00000000  .00000000  00000-0  00000-0 0  9991
2 99003   0.2589 270.0016 0096595 270.0000   0.0000  0.03589863    08
```

Combined GENESIS and NovaMoon TLE

```
GENESIS_TARGET
1 99001U 26001A   26001.00000000  .00000000  00000-0  00000-0 0  9997
2 99001  95.5000   0.0000 0000000   0.0000 180.0000  6.30950882    00
NOVAMOON_TARGET
1 99003U 26003A   26001.00000000  .00000000  00000-0  00000-0 0  9991
2 99003   0.2589 270.0016 0096595 270.0000   0.0000  0.03589863    08
```

Department of Physics and Astronomy
CHALMERS UNIVERSITY OF TECHNOLOGY
Gothenburg, Sweden
www.chalmers.se

CHALMERS
UNIVERSITY OF TECHNOLOGY